

Article

TurboID-Based IRE1 Interactome Reveals Participants of the Endoplasmic Reticulum-Associated Protein Degradation Machinery in the Human Mast Cell Leukemia Cell Line HMC-1.2

Nabil Ahmed ¹, Christian Preisinger ², Thomas Wilhelm ¹ and Michael Huber ^{1,*} 

¹ Institute of Biochemistry and Molecular Immunology, Medical Faculty, RWTH Aachen University, 52074 Aachen, Germany; twilhelm@ukaachen.de (T.W.)

² Proteomics Facility, Interdisciplinary Centre for Clinical Research (IZKF), RWTH Aachen University, 52074 Aachen, Germany; cpreisinger@ukaachen.de

* Correspondence: mhuber@ukaachen.de

Abstract: The unfolded protein response is an intricate system of sensor proteins in the endoplasmic reticulum (ER) that recognizes misfolded proteins and transmits information via transcription factors to either regain proteostasis or, depending on the severity, to induce apoptosis. The main transmembrane sensor is IRE1 α , which contains cytoplasmic kinase and RNase domains relevant for its activation and the mRNA splicing of the transcription factor XBP1. Mast cell leukemia (MCL) is a severe form of systemic mastocytosis. The inhibition of IRE1 α in the MCL cell line HMC-1.2 has anti-proliferative and pro-apoptotic effects, motivating us to elucidate the IRE1 α interactors/regulators in HMC-1.2 cells. Therefore, the TurboID proximity labeling technique combined with MS analysis was applied. Gene Ontology and pathway enrichment analyses revealed that the majority of the enriched proteins are involved in vesicle-mediated transport, protein stabilization, and ubiquitin-dependent ER-associated protein degradation pathways. In particular, the AAA AT-Pase VCP and the oncoprotein MTDH as IRE1 α -interacting proteins caught our interest for further analyses. The pharmacological inhibition of VCP activity resulted in the increased stability of IRE1 α and MTDH as well as the activation of IRE1 α . The interaction of VCP with both IRE1 α and MTDH was dependent on ubiquitination. Moreover, MTDH stability was reduced in IRE1 α -knockout cells. Hence, pharmacological manipulation of IRE1 α -MTDH-VCP complex(es) might enable the treatment of MCL.

Keywords: ERAD pathway; mastocytosis; metadherin; ubiquitination; valosin-containing protein



Citation: Ahmed, N.; Preisinger, C.; Wilhelm, T.; Huber, M. TurboID-Based IRE1 Interactome Reveals Participants of the Endoplasmic Reticulum-Associated Protein Degradation Machinery in the Human Mast Cell Leukemia Cell Line HMC-1.2. *Cells* **2024**, *13*, 747. <https://doi.org/10.3390/cells13090747>

Academic Editor: Alessandro Poggi

Received: 14 December 2023

Revised: 2 April 2024

Accepted: 17 April 2024

Published: 25 April 2024



Copyright: © 2024 by the authors. Licensee MDPI, Basel, Switzerland. This article is an open access article distributed under the terms and conditions of the Creative Commons Attribution (CC BY) license (<https://creativecommons.org/licenses/by/4.0/>).

1. Introduction

Mast cells (MCs) are crucial regulators of inflammatory processes via the production and release of various mediators (e.g., histamine, proteases, arachidonic acid metabolites, cytokines, chemokines, and growth factors [1]). Abnormal growth and/or activation of MCs in various tissues is pathophysiological. Systemic mastocytosis (SM) is a rare and heterogeneous disorder characterized by the unusual accumulation of MCs in the bone marrow or in multiple organ systems including the skin, digestive tract, and liver, amongst others [2,3]. Patients diagnosed with the indolent form of SM mainly suffer from the effects of hyper-release of MC mediators, while the aggressive form of SM is closely linked to the development of organ damage and a significantly diminished overall survival rate.

MC leukemia (MCL) is the most aggressive form of SM, and is characterized by a dramatic increase in MC numbers in the bone marrow and peripheral blood. The presence of KIT^{D816V} is a prominent characteristic mutation observed in over 80% of patients with SM, resulting in constitutive, ligand/stem cell factor-independent activation of the receptor tyrosine kinase KIT. In addition, KIT^{D816V} can be detected in other myeloid lineages in advanced stages of SM [4–6]. Although KIT^{D816V} is resistant to the tyrosine kinase inhibitor

(TKI) imatinib, several TKIs (e.g., midostaurin) [7] have been identified as potent inhibitors. Nevertheless, therapy using TKIs is often accompanied by severe side effects and acquired resistance. Therefore, additional strategies to target neoplastic MCs have to be developed.

In particular, in situations of enhanced proliferation and/or protein production, such as the growth of cancer cells and cytokine secretion from immune cells, adaptive control of proteostasis is essential. Previously, we have shown that the unfolded protein response (UPR) is a pro-survival pathway of the MCL cell line HMC-1.2 [8].

The UPR utilizes the ER stress sensors inositol-requiring enzyme 1 α (IRE1 α ; gene name: *ERN1*), eukaryotic initiation factor 2 α (eIF2 α) kinase (PERK), and activating transcription factor 6 (ATF6) to recognize the accumulation of misfolded proteins in the ER. IRE1 α is an ER-located type I transmembrane protein with catalytic endonuclease (RNase) and kinase activities in its cytosolic domain [9]. In response to ER stress, IRE1 α cleaves the mRNA coding for the X-box-binding protein 1 (*XBP1*), resulting in its spliced form (*XBP1s*), which encodes an active transcription factor. *XBP1s* translocates into the nucleus and controls the transcription of a large number of UPR target genes, amongst them are genes encoding proteins involved in ER-associated protein degradation (ERAD) [10,11]. In the course of the ERAD process, misfolded luminal and transmembrane ER proteins are retro-translocated from the ER, which are then ubiquitinated and extracted and then degraded within the 26S proteasome [12]. The molecular force required for extraction and unfolding is provided by valosin-containing protein (VCP), which belongs to the group of AAA ATPases, and can be seen as the main executor of the ERAD machinery [13]. The ER transmembrane protein metadherin (MTDH) has been characterized as an oncogene that affects several signaling pathways and transcription factors, such as RAS, MYC, PI3K/AKT, NF κ B, mitogen-activated protein kinase, and WNT [14]. It has been identified as a functional driver in multiple aspects of cancer progression, promoting cancer cell proliferation and resistance to treatment by acting as an RNA-binding protein [15]. Most likely, misfolded MTDH or homeostatically removed MTDH is processed by the activity of VCP, suggesting functional and/or local interactions between these proteins.

Depending on the strength and/or duration of the ER stress, IRE1 α is activated by dimerization or oligomerization. Moreover, several interactors have been identified to regulate the function of IRE1 α [16]. Hence, IRE1 α in a context-driven manner can regulate the adaptive arm of the UPR as well as promote the terminal UPR leading to apoptosis [9]. In contrast to the ubiquitously expressed IRE1 α , its paralogue, IRE1 β (gene name: *ERN2*), is considered to be specifically expressed in the epithelial cells of mucosal surfaces and is a less efficient transducer of the UPR, and may function as a negative regulator of IRE1 α [17,18].

However, despite the substantial contribution of IRE1 α in maintaining ER homeostasis and the knowledge on its numerous interactors, there remains a considerable gap in the comprehension of its functions in the cancer framework, necessitating further investigation. Recently, several studies reported that IRE1 α is an essential regulator of migration, invasion, and metastasis in diverse types of cancer [19–21]. Consequently, further investigation is needed to enhance our understanding of the biological role of IRE1 α in cancer progression and its associated pathological mechanisms [22].

In this study, we aimed to identify IRE1 α and IRE1 β interaction partners that are involved in regulation of IRE1 function in the MCL model system of HMC-1.2 cells. We conducted an independent proteomic screen utilizing proximity-dependent biotin identification (TurboID) using IRE1 as the bait. Our analysis showed that the predominant interacting proteins in HMC-1.2 cells were consistently bound to IRE1 α and mostly unaffected by the presence of additional ER stress conditions. In particular, we found that the stability of IRE1 α and the ER transmembrane protein MTDH is dependent on VCP. Furthermore, the presence of IRE1 α could strengthen the initial stability of MTDH which might play a crucial role in the progression of MCL.

2. Materials and Methods

2.1. Cell Culture

HMC-1.2 (KIT^{V560G,D816V}) and HMC-1.1 (KIT^{V560G}) cells were kindly provided by Dr. J. Butterfield (Mayo Clinic, Rochester, MN, USA) [23]. T84 cells used in this study were generously provided by Prof. Dr. Jörg Schulzke (Charité, Berlin, Germany). Jurkat, K562 and HEK-293T were acquired from ATCC (American Type Culture Collection, Manassas, VA, USA).

T84 cells were grown in DMEM-F12 (Gibco, Thermo Fisher Scientific, Waltham, MA, USA, #10565018) and HEK293 in DMEM (Gibco, Thermo Fisher Scientific, Waltham, MA, USA, #10569010) supplemented with 10% fetal bovine serum (FBS) (Capricorn, Duesseldorf, Germany #FBS-12A), 50 units/mL penicillin and 50 ng/mL streptomycin (Sigma-Aldrich, Darmstadt, Germany, #P4333). All other cell lines were cultured in RPMI 1640 medium (Invitrogen, Dreieich, Germany, #21875-0991) supplemented with 10% FBS, 50 units/mL penicillin and 50 ng/mL streptomycin in an atmosphere containing 5% CO₂. The medium was renewed twice a week.

2.2. Plasmid Constructs

General molecular biology reagents, including restriction enzymes, Phusion HF DNA Polymerase (#, M0530) and Quick Ligation Kit (#M2200), were from New England Biolabs (Frankfurt, Germany). DH5 α competent cells were provided by the Institute of Biochemistry, Hospital University of Aachen. QIAquick gel extraction (#M0530) and DNA purification kits (#51306/#12662) were from Qiagen (Hilden, Germany).

The following plasmid were used in this study:

Flag_HsIRE1a_pBabePuro was a gift from David Ron (Addgene plasmid #54337; <http://n2t.net/addgene:54337> (accessed on 22 February 2019); RRID: Addgene_54337) and has been described in Volmer et al. [24]. Flag_HsIRE1 α _delta589-903 was generated from Flag_HsIRE1 α _pBabePuro. The IRE1 α kinase-dead (KD) construct hIRE1 α K599A was a gift from Fumihiko Urano (Addgene plasmid #20745; <http://n2t.net/addgene:20745> (accessed on 22 February 2019); RRID: Addgene_20745) [25].

pBabe-puro was a gift from Hartmut Land and Jay Morgenstern and Bob Weinberg (Addgene plasmid #1764; <http://n2t.net/addgene:1764> (accessed on 22 February 2019); RRID: Addgene_1764) [26].

V5-TurboID-NES_pCDNA3 was a gift from Alice Ting (Addgene plasmid #107169; <http://n2t.net/addgene:107169> (accessed on 2 April 2024); RRID: Addgene_107169) [27].

pUMVC (Addgene plasmid # 8449; <http://n2t.net/addgene:8449> (accessed on 24 April 2020); RRID: Addgene_8449) and pCMV-VSV-G (Addgene plasmid #8454; <http://n2t.net/addgene:8454> (accessed on 2 April 2024); RRID: Addgene_8454) were a gift from Bob Weinberg [28]

pSpCas9(BB)-2A-Puro (PX459) V2.0 was a gift from Feng Zhang (Addgene plasmid #62988; <http://n2t.net/addgene:62988> (accessed on 2 April 2020); RRID: Addgene_62988) [29].

VCP(wt)-EGFP was a gift from Nico Dantuma (Addgene plasmid #23971; <http://n2t.net/addgene:23971> (accessed on 2 April 2024); RRID: Addgene_23971) [30].

Human ERN2 construct coding sequences were PCR amplified from ERN2 templates (provided by K. Kohno, Nara Institute of Science and Technology, Ikoma, Japan) [31] using primers with NaeI and AgeI restriction sites for the insertion into pBabe-puro [26].

Expression constructs coding for ERN1 or ERN2 fused to C-terminal TurboID were generated by restriction enzyme-based molecular cloning using the AgeI and XhoI restriction sites from V5-TurboID-NES_pCDNA3 [27].

CRISPR–Cas9-mediated gene knockouts of human ERN1 and ERN2 were performed using the pSpCas9(BB)-2A-Puro (PX459) V2.0 plasmid (Ran et al., 2013) containing gRNA for IRE1 α (5'-CTTTTATGTCTGGCAGCGGG-3') and gRNA for IRE1 β (5'-GCTGAGCAACT CACCGTAGT-3'). Pairs of oligonucleotides with a BbsI overhang were annealed and then ligated into the BbsI-digested vector.

2.3. Mammalian Cell Transfections

Transient plasmid transfections of HEK293 cells were performed using the transfection reagent TransIT-LT1 (MirusBio, Madison, WI, USA, #731-0029) according to the manufacturer's instructions. Generally, 1 µg of MSCV-GFP plasmid encoding GFP was co-transfected as a control to verify that the transfection efficiency was around 80% in all wells. Transfected cells were usually cultured for 24–48 h before further manipulation or analysis. The stable cell lines were generated by retroviral transductions. First, HEK293T cells were transfected with a mixture of DNA containing 1 µg of pBABE-puro target, 0.9 µg of pUMVC packaging, and 0.1 µg pCMV-VSV-G envelope plasmids using the TransIT-LT1 transfection reagent. The supernatant of the transfected cells was collected 48 h later and filtered through a 0.45 µm pore filter. For viral infection, the virus-containing supernatants from HEK293T cultures were mixed with polybrene (Sigma-Aldrich, Darmstadt, Germany, #TR-1003) to a final concentration of 8 µg/mL and were added to HMC-1.2 or HEK293 cells. Together with the viral supernatant, the cells were centrifuged at 1000 g for 1.5 h at room temperature (RT) and the medium was renewed. This step was repeated two more times every 24 h. Then, the cells were returned to a CO₂ incubator, and 72 h later, the cells were selected in 2.5 µg/mL puromycin (Sigma-Aldrich, #P8833).

The cell lines HMC-1.2^{Flag-IRE1α}, HMC-1.2^{IRE1α-TurboID}, HMC-1.2^{IRE1β-TurboID}, and HMC-1.2^{V5-TurboID} were generated by stable transduction of HMC-1.2^{IRE1-/-} cells. HEK293^{Flag-IRE1α} was generated by stable transduction of HEK293^{IRE1α-/-} cells.

2.4. Pharmacological Inhibitors and ER Stress Inducers

To induce ER stress, cells were exposed to 5 µg/mL tunicamycin (TM, Applichem, Darmstadt, Germany, #A2242), 100 nM thapsigargin (Tg, Abcam, Cambridge, UK, #ab120286), or 10 nM bortezomib (BZ, Selleckchem, Cologne, Germany, #S1013) for the indicated period. 20 µM of the E1 ubiquitin-activating enzyme inhibitor MLN7243 (MedChemExpress, Junction, NJ, USA, #HY-100487) was used to prevent ubiquitination.

For the cycloheximide (CHX) chase experiments, HMC-1.2 cells were treated with 50 µg/mL CHX (Sigma-Aldrich, #01810) for the indicated times. VCP activity was inhibited by CB-5083 (#19311) or NMS-873 (#17674) (1 µM; both from Cayman, Ann Arbor, MI, USA).

2.5. RNA Preparation and Quantitative RT-PCR

RNA from 2 × 10⁶ HMC-1.2 cells was extracted using a NucleoSpin RNA Plus Kit (Macherey Nagel, Dueren, Germany, #740955.50) according to the manufacturer's instructions. Total RNA (1 µg) was reverse transcribed using random oligonucleotides (Roche, Merck, Darmstadt, Germany #11034731001) and an Omniscript Kit (Qiagen, #205113) according to the manufacturer's instructions. qPCR was performed on a Rotorgene (Qiagen) by using the SYBR green reaction mix SensiFast (Meridian Biosciences, Cincinnati, OH, USA, #QT650-02). The primers used for PCR amplification were as follows:

XBP1s fwd CTGAGTCCGAATCAGGTGCGAG, rev: GAAGAGTCAATACCGCCA-GAAT; *DNAJB4* fwd GGAAGGAGGAGCGCTAGGTC, rev ATCCTGCACCCTCCGACTAC; *HSPA5* fwd TGACATTGAAGACTTCAAAGCT, rev CTGCTGTATCCTCTTACCAGT; *ATF4* fwd GCTAAGGCGGGCTCCTCCGA, rev ACCCAACAGGGCATCCAAGTCAA; *CHOP* fwd GGAGCATCAGTCCCCACTT, rev TGTGGGATTGAGGGTCACATC; *PPP1R15A* fwd GAGGAGGCTGAAGACAGTGG, rev AATTGACTTCCCTGCCCTCT; *ATF6* fwd CGAAGGGATCACCTGCTGTT, rev, CCTGGTGTCCATCACCTGAC; *XBP1u* fwd CAGCACTCAGACTACGTGCA, rev ATCCATGGGGAGATGTTCTGG; *EDEM1* fwd CC ACTGAGACCAGACTTAGTG, rev CGTACCCACACTTGACTTTTGTG; *ERN1* fwd TGCT-TAAGGACATGGCTACCATCA, rev, CTGGAAGTCTGGTGGTGGGA; *ERN2* fwd TCGAAG-GACCAATGTACGTCA, rev GGATGGTGAATGGCAGTTTCAT; *HPRT* fwd TGACACTG-GCAAACAATGCA, rev GGTCCTTTTCACCAGCAAGCT. All quantitative RT-PCR reactions were performed in triplicate. Transcript expression was normalized to the house-keeping gene *HPRT* and relative expression was calculated according to the delta-CT method [32].

2.6. TurboID, Biotinylation Assay, and Mass Spectrometry

TurboID was performed as described previously [27] with minor modifications. In the beginning, 30×10^6 HMC-1.2^{IRE1 α -/-} cells expressing different constructs of IRE1 α -TurboID fusion proteins were cultivated in medium supplemented with the solvent control DMSO or tunicamycin for 2 h. Subsequently, 500 μ M biotin (Sigma-Aldrich, #B4501) was added to the medium to promote proximity biotinylation for 1 h. After the incubation period, the cells were rinsed three times in phosphate-buffered saline (PBS) and then subjected to lysis using RIPA buffer (50 mM Tris-HCl pH 7.5, 250 mM NaCl, 1% Triton X-100, 1 mM DTT, 0.5% Na-deoxycholate, and 1mM PMSF), supplemented with protease inhibitors (20 μ g/mL aprotinin, 4 μ g/mL leupeptin) and incubated on a rotator for 1 h at 4 °C. The lysates were then transferred into 1.5 mL reaction tubes and sonicated in an ice bath three times with a 30% duty cycle for 20 s with 1.5 min breaks on ice. The suspension was centrifuged for 15 min at 4 °C and $16.500 \times g$ to remove the cell debris and the clear supernatant was applied to a PD-10 desalting column (Cytiva, Dreieich, Germany, #17085101) to remove the excess free biotin using the gravity protocol according to the manufacturer's instructions. Proteins were eluted with 1 mL of lysis buffer. The protein concentration of the protein extract was measured using a BCA protein assay kit (PierceTM, Thermo Fisher Scientific, #23225). To enrich for biotinylated proteins from the protein extracts, 250 μ L of streptavidin magnetic beads (PierceTM, Thermo Fisher Scientific, #88817) were washed twice with wash buffer (lysis buffer without protease inhibitors and PMSF), and desalted lysates containing 3 mg protein were then incubated with the beads on a rotator overnight at 4 °C. The beads were washed twice with 1 mL of wash buffer. To completely remove the detergent, the beads were washed once in 1 mL of 1 M KCl for 2 min, then 0.1 M Na₂CO₃ for 10 s, and lastly with 2 M urea in 10 mM Tris-HCl pH 8.0 for 10 s. Finally, the beads were resuspended in 1 mL of final buffer (50 mM Tris-HCl pH 7.5 and 250 mM NaCl). To confirm the successful enrichment of the biotinylated proteins, 5% of the washed streptavidin beads were used for analyses by silver staining gel, and the remaining beads were flash-frozen in liquid nitrogen and stored at -80 °C until the LC-MS/MS analysis.

For the mass spectrometry analysis, the co-immunoprecipitates/TurboID precipitates were washed three times with lysis buffer w/o detergent. The samples were then prepared as described previously [33]. The resulting lyophilized peptides were resuspended in 15 μ L of 3% formic acid (FA)/5% acetonitrile (ACN) and 5 μ L were loaded onto a nanoLC system (RSLCnano, Thermo Fisher Scientific, Bremen, Germany). Prior to separation, the peptides were subjected to trapping on a pre-column (Acclaim PepMap100, C18, 5 μ m, 100 Å, 300 μ m i.d. \times 5 mm, Thermo Fisher Scientific, Bremen, Germany). The analytes were then separated on an analytical column (Easyspray 50 cm column (ES803) at 45 °C; Thermo Fisher Scientific, Bremen, Germany) using a 70 min gradient run at 250 nL/min (0–10 min: 5% buffer B (buffer A: 0.1% FA; buffer B: 80% acetonitrile, 0.1% FA); 10–42 min: 5–35% buffer B; 42–47 min: 35–99% buffer B; 47–52 min: 99% buffer B; 52–55 min: 99–5% buffer B; 55–70 min: 5% buffer B). The eluting peptides were analyzed on a Q Exactive plus mass spectrometer (250 °C capillary temperature, 2 kV spray voltage; Thermo Fisher Scientific, Bremen, Germany) in data-dependent mode. The full MS settings were as follows: resolution, 70,000; AGC target, 2×10^5 ; maximum injection time, 100 milliseconds; scan range, 300–1650 m/z . The dd-MS2 settings were as follows: resolution, 17,500; AGC target, 2×10^5 ; maximum injection time, 110 milliseconds; top 10 precursor fragmentation; isolation window, 1.8 m/z ; collision energy, 27. The dd settings were as follows: minimum AGC, 5×10^2 ; 10 s dynamic exclusion; only 2+ to 5+ peptides were allowed.

The raw data from the Orbitrap instrument were analyzed with MaxQuant (MQ, version 2.0.1.0) with the built-in Andromeda search engine [34]. The search was conducted against the human UniProt database (version 04/2021; with only reviewed and canonical sequences being used) and MQ default settings. The specific settings were protease: trypsin (two missed cleavages allowed); fixed modification: carbamidomethylation (Cys); variable modifications: oxidation (Met) and N-terminal protein acetylation; false discovery rate: 0.01

(both peptide and protein levels); minimum peptide length: seven amino acids. Relative quantification was carried out by utilizing the label-free quantitation algorithm from MQ.

The resulting proteinGroups.txt file was further analyzed using the Perseus suite (version 1.6.14.0; [35]). The three biological replicates of the six experimental conditions (IRE1 α , IRE1 β , and con (plus DMSO or tunicamycin) were grouped into three groups (IRE1 α , IRE1 β , and con) resulting in six “replicates” per condition (see main text for explanation). The protein list was then filtered for reversed hits, contaminants, and “only identified by site” entries. Furthermore, a protein was required to be identified by a minimum of two unique peptides for further evaluation. The data were log₂-transformed and filtered for proteins that were identified in all six replicates of one of the three groups; afterwards, standard imputation of missing values was performed. An additional analysis was carried out using the two-sample tests feature in Perseus. These files were then used to generate the volcano plot (Instant Clue, [36], Venn diagram (<https://bioinfogp.cnb.csic.es/tools/venny/> (accessed on 2 April 2024)) and string enrichment analysis (Cytoscape 3.10.0; stringApp 2.0.1).

2.7. Immunoprecipitation, Immunoblotting, and Antibodies

Cells were lysed in RIPA buffer and centrifuged for 10 min at 16,500 \times g. The supernatant of the lysates were then incubated with anti-Flag M2 Magnetic beads (Sigma, #M8823) or anti-GFP-Trap Magnetic Agarose (ChromoTek, Proteintech, Planegg-Martinsried, Germany, #gtma) for the indicated period at 4 °C. Subsequently, the beads were washed five times in wash buffer and eluted by boiling in 2 \times SDS sample buffer. The protein samples were separated by SDS-PAGE and transferred to PVDF membranes (Thermo Fisher Scientific, #88518). The blots were blocked for 30 min at RT in TBS-T buffer (50 mM Tris (pH 7.4), 150 mM NaCl, 0.1% Tween-20) containing 5% bovine serum albumin and then incubated with the selected antibody solutions. Immunoblot analysis was performed with the indicated antibodies and visualized by chemiluminescence (ImageQuant™ LAS 4000, GE Healthcare, Chicago, IL, USA). The following antibodies were used: anti-IRE1 α (#14C10), anti-BIP (#3183), anti-VCP (#2648), and anti-ubiquitin (#3936), which were purchased from Cell Signaling Technology (Leiden, The Netherlands); anti-MTDH (#40-6500), anti-VCP (#MA3-004), and anti-streptavidin HRP (#21130), which were purchased from Thermo Fisher Scientific; anti-phospho-IRE1 α S724, which was purchased from Novus (#2323SS); anti-GAPDH (#sc-32233), which was from Santa Cruz Biotechnology (Heidelberg, Germany); anti-vinculin (#V9131) and anti-FLAG M2 (#F1804), which were from Sigma-Aldrich (Darmstadt, Germany); anti-GFP, which was from Rockland (#600-101-215); anti-VAPA which was from Ptglab (ChromoTek, Martinsried, Germany, 15275-1-AP); and anti-emerin, which was a gift from Wolfram Antonin (Institute of Biochemistry and Molecular Cell Biology). HRP-coupled secondary antibodies were purchased from Agilent (Dako, Waldbronn, Germany, #P0448 and P0447).

2.8. Densitometric Analysis

To quantitatively analyze the protein bands from the Western blot images, ImageJ software 1.53k was used following a structured procedure. The recommendations of the National Institutes of Health (NIH) protocol (<https://imagej.net/ij/nih-image/manual/tech.html> (accessed on 2 April 2024)) were followed. The obtained quantitative data were exported to the Excel program for further analysis. Normalization was achieved by dividing the intensities of the test protein (e.g., MTDH) by the respective intensities of the control protein (e.g., vinculin). This process assists in normalizing the data across samples and eliminates any background signals from the protein signal. Comparative expression levels were determined by calculating the ratio of normalized values between test samples (after treatment) and control sample (untreated), which were then standardized to a value of 1 (untreated sample).

2.9. Immunofluorescence (IF)

HEK-293 cells were cultured in twelve-well plates with glass coverslips until they reached 30–40% confluency. The cells were washed and fixed with 4% paraformaldehyde, permeabilized with 0.1% Triton X-100 in PBS, and blocked with 5% bovine serum albumin in PBS containing 0.1% Triton X-100. Then, the cells were incubated with rabbit anti-calnexin (#2679, CST) primary antibody at 4 °C overnight. After washing, the cells were stained with anti-DYKDDDDK tag (#MA1-142-A488, Invitrogen) to detect Flag-IRE1 α and Alexa Fluor 594-conjugated anti-rabbit IgG (A-11012, Invitrogen) to detect calnexin for 1 h at room temperature. After washing, fluorescent signals were detected under a confocal microscope [FV1000; Olympus, Hamburg, Germany; equipped with a photomultiplier (model R7862; Hamamatsu)].

2.10. Statistical and Bioinformatic Analysis

All data shown were generated from at least three independent experiments. The statistical analysis and graphing of data were performed using GraphPad Prism 10 Version 10.2.2 (GraphPad Software, San Diego, CA, USA, 92108). All statistical test procedures were performed as described in the respective figure legends. *p*-values were considered statistically significant according to the GP style in GraphPad Prism (ns: $p > 0.05$, * $p < 0.05$, ** $p < 0.01$, *** $p < 0.001$, **** $p < 0.0001$). The respective number of independent biological replicates per experiment are indicated in the figure legends. To address the quantitative aspects of the proteomic data, we utilized the MetaboAnalystR package (version 3.1.0) to compare the label-free quantitation (LFQ) intensity between the IRE1 groups and the control group. In addition to the comparative analysis, we employed the UniProtR package (version 2.2.2), which allowed us to perform a comprehensive Gene Ontology (GO) analysis, enriching our understanding of the biological pathways affected by the observed perturbations.

3. Results

3.1. UPR Activation in IRE1 α - and IRE1 β -Deficient HMC-1.2 Cell Lines

Maintaining proteostasis is particularly essential for the proliferation and survival of cancer cells, which are therefore strongly dependent on a functional UPR. We have shown previously that the induction of proteotoxic ER stress in the MCL cell line HMC-1.2 activates the mechanisms of a terminal UPR [8]. Although the RNase domain of IRE1 α is the main executor of *XBP1* splicing, a significant amount of spliced *XBP1* was still detectable in IRE1 α -deficient cells upon induction of ER stress using thapsigargin (Tg) (Figure S1A). The Tg-induced production of PERK-dependent *CHOP* (*DDIT3*) was not affected by IRE1 α deficiency (Figure S1B). This might suggest a selective role of the second IRE1 isoform, IRE1 β . To date, IRE1 β expression was only reported in non-ciliated cells, such as intestinal epithelial cells and airway mucous cells in humans [17]. Thus, we analyzed the relative mRNA expression of IRE1 β in different human cell lines, including human MC lines. While IRE1 β was notably detectable in the human colon carcinoma cell line T84 [18], a lower amount of mRNA expression was detectable in all analyzed cell lines, suggesting a potential role in HMC-1.2 cells (Figure S1C).

To elucidate the biological implications of both IRE1 isoforms in an MCL model system, single IRE1 α -, single IRE1 β -, and double IRE1 α/β -deficient HMC-1.2 cells were generated using CRISPR/Cas9 gene editing. Importantly, compared to the parental cells, the expression of IRE1 β mRNA was strongly reduced in both deficient cell lines, HMC-1.2^{IRE1 β -/-} and HMC-1.2^{IRE1 α/β -/-} (Figure S1D), proving the specificity of the primers used for the RT-qPCR analysis.

Tunicamycin (TM), a potent ER stressor that inhibits N-linked glycosylation and thus causes aggregation of misfolded membrane or secreted proteins, was used to evaluate the ER stress response in the IRE1-deficient cell variants compared to the parental HMC-1.2 cells. The expression of UPR target genes measured by RT-qPCR confirmed that TM was able to activate all three arms of the UPR (IRE1 α , PERK, and ATF6) in the parental HMC-1.2 cells.

TM activated the target genes in the IRE1 pathway (*XBP1s*, *DNAJB4*, and *HSPA5*), PERK pathway (*ATF4*, *CHOP*, and *PPP1R15A*), and ATF6 pathway (*ATF6*, *us-XBP1*, and *EDEM1*). Notably, *HSPA5* is a target gene of the ATF6 pathway as well. IRE1-dependent splicing of *XBP1* (Figure 1A) and the expression of the *XBP1s* target gene *DNAJB4* (Figure 1B) were strongly reduced in IRE1 α single- as well as IRE1 α/β double-deficient cells. Interestingly, the single deletion of IRE1 β alone also reduced *XBP1* splicing, suggesting a contribution of IRE1 β in *XBP1* splicing while *DNAJB4* expression was not significantly affected. The expression of *HSPA5* (coding for BIP, Figure 1C), a common target gene of both *XBP1s* and ATF6f, was not affected by IRE1 depletion, suggesting a dominant role of ATF6f. Although IRE1 was depleted in the generated HMC-1.2 cell lines, the activation of the PERK and ATF6 pathways was not further enhanced by compensatory mechanisms, as measured by the expression of *ATF4* (Figure 1D), *DDIT3* (coding for CHOP, Figure 1E), and *PPP1R15A* (coding for GADD34, Figure 1F). While the increases in *ATF4* and *CHOP* expression induced by TM were comparable in the parental and IRE1-deficient cell lines, *PPP1R15A* was induced to a smaller degree in all IRE1-deficient cells, suggesting another function of IRE1 α and/or IRE1 β in MCL cells. Although *ATF6* (Figure 1G) expression was not increased after 3 h of TM treatment, the ATF6f target gene *us-XBP1* (Figure 1H) was significantly increased in all studied cell lines. Finally, the expression of the ERAD marker *EDEM1* was not induced by TM application in the cell lines under study (Figure 1I). In conclusion, IRE1-deficient HMC-1.2 cell lines showed a comparable activation of IRE1-independent UPR target genes. Interestingly, IRE1 β appears to contribute to TM-induced *XBP1* splicing.

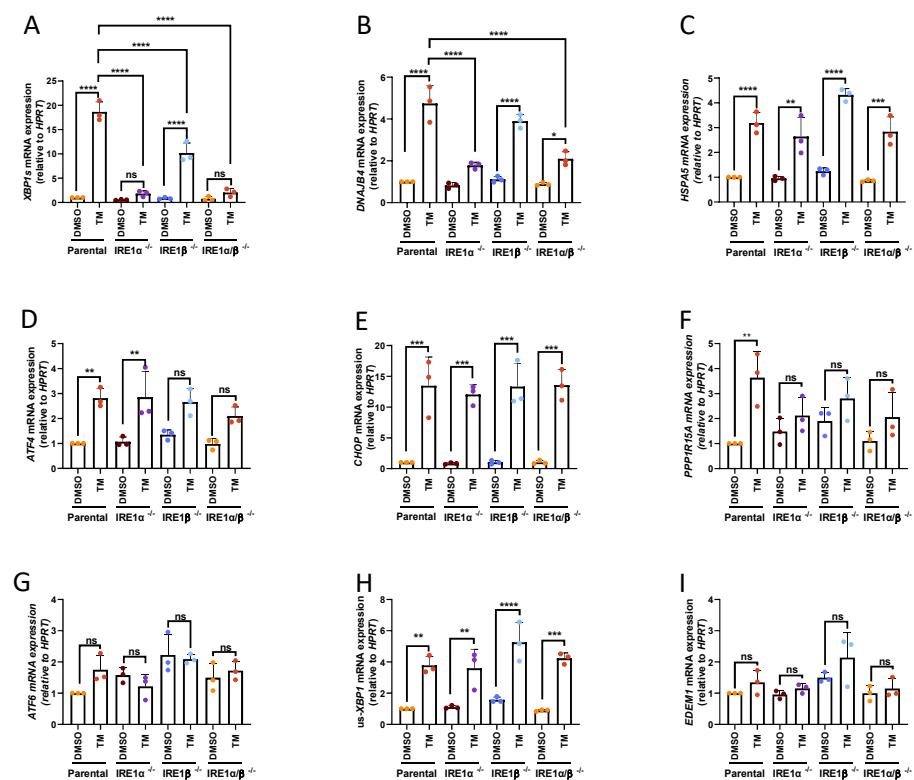


Figure 1. UPR activation in IRE1 α - or IRE1 β -deficient HMC-1.2 cell lines. Parental and IRE1-deficient (IRE1 α $^{-/-}$, IRE1 β $^{-/-}$, IRE1 α/β $^{-/-}$) HMC-1.2 cells were treated with vehicle (DMSO) or 5 μ g/mL TM for 3 h. Deficiency in IRE1 α protein in HMC-1.2^{IRE1 α $^{-/-}$} cells is shown in Figure 6. The expression of UPR target genes in the IRE1 pathway ((A) *XBP1s*, (B) *DNAJB4*, and (C) *HSPA5*), the PERK pathway ((D) *ATF4*, (E) *CHOP*, and (F) *PPP1R15A*), and the ATF6 pathway ((G) *ATF6*, (H) *usXBP1*, and (I) *EDEM1*) was evaluated by RT-qPCR and normalized to *HPRT* ($n = 3$). Data shown as mean \pm SD. Significance levels are based on one-way ANOVA. * $p < 0.05$, ** $p < 0.01$, *** $p < 0.001$ **** $p < 0.0001$, ns not-significant.

3.2. Identification of IRE1 Interacting Proteins Using a TurboID Approach

The accumulation of misfolded proteins in the ER causes the dimerization or oligomerization of IRE1, leading to the activation of its cytoplasmic kinase and RNase domains. Although this activation is mainly mediated by BIP dissociation, several interacting proteins have been identified in the regulation of IRE1 function [37].

The current study was designed to identify potential regulators of IRE1 function by employing the TurboID proximity labeling technique to discern IRE1 α and IRE1 β interaction proteomes in the HMC-1.2 cell line. Therefore, IRE1 α -deficient HMC-1.2 (HMC-1.2^{IRE1 α -/-}) cells were stably transduced with IRE1 constructs containing the BirA-variant TurboID fused to the IRE1 C-terminus (Figure 2A). Initially, the subcellular location of overexpressed IRE1 α -TurboID was validated in the ER using fluorescence microscopy in HEK293 cells, demonstrating co-staining of FLAG-tagged hIRE1 α -TurboID with the ER marker calnexin (Figure S2A). Moreover, ER stress-induced S724 phosphorylation of FLAG-tagged IRE1 α -TurboID was comparable to the signal of heterologously expressed FLAG-tagged IRE1 α (Figure S2B). The expressed IRE1 α -TurboID or IRE1 β -TurboID fusion proteins were used as bait proteins to specifically focus on proteins that bind in the cytosol. The interactomes were compared to the cytosolic empty vector control V5-TurboID under non-stressed and ER stress (induced with TM for 2 h) conditions before biotin was supplemented for 1 h to facilitate proximal protein biotinylation (see Figure 2A for work pipeline). Biotinylated proteins were enriched using a streptavidin column. A small portion of enriched proteins was used to compare the respective patterns by silver staining before the samples were subjected to LC-MS/MS (Figure 2A).

The MS analysis identified a total number of 1232 proteins present in at least one sample. Following data processing, which included contaminant filtering and log₂ transformation, we derived a final count of 624 proteins. The Label-Free Quantification (LFQ) intensity was determined for all identified proteins. The LFQ intensities showed a high Pearson correlation among replicates. However, the correlation coefficient between the IRE1 α and IRE1 β samples was approximately 0.5, reflecting their high similarity (Figure S2C, Datafile S1). A Principal Component Analysis (PCA) of significant proteins indicated a distinct separation between the two IRE1 isoforms and the control group, albeit without a noticeable variance between unstressed and ER stress conditions (Figure 2B). Therefore, we decided to merge the DMSO- and TM-treated groups. Following an overlap analysis of the protein candidates identified in the TurboID/MS analysis, 194 IRE1-interacting proteins were identified within all IRE1 constructs under non- and ER-stressed conditions (Figure 2C).

In addition, hierarchical clustering of the top 250 overrepresented proteins showed distinguishable patterns among the groups, especially between the cytoplasmic control and the IRE1 isoforms. Again, no clear separation between the DMSO and TM treatments were observed (Figure 2D), which supports our previous observation of an already activated UPR under basal conditions in HMC-1.2 cells [8].

The major changes that met the criteria of the quantitative MS analysis between IRE1 α and control (Figure 2E) and between IRE1 β and control (Figure S1E) are depicted in volcano plots.

Interestingly, the subsequent STRING analysis of the specific IRE α interactors and Gene Ontology (GO) and pathway enrichment analyses of the candidate proteins revealed that the majority of the enriched proteins have an ER localization and are involved in ER stress responses and ER to Golgi vesicle-mediated transport (Figure 2D–F).

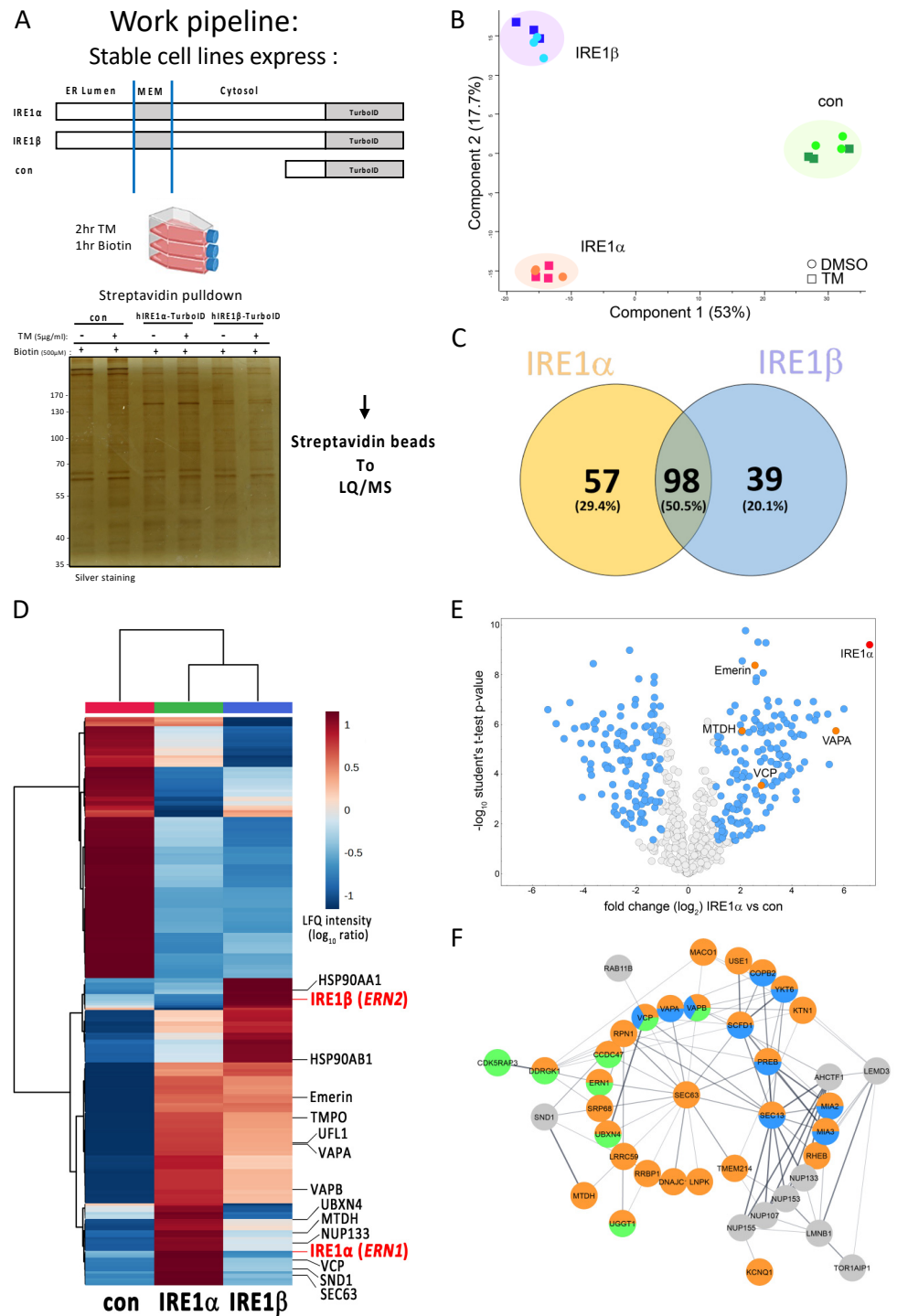


Figure 2. Identification of IRE1-interacting proteins with TurboID. (A) Generation of IRE1 α -TurboID constructs and TurboID assay workflow. Schematic representation of IRE1 constructs and V5 control. TurboID was fused to the C-terminal domain of both human IRE1 α (IRE1 α -TurboID) and human IRE1 β (IRE1 β -TurboID). Parental HMC-1.2 and HMC-1.2^{IRE1 α -/-} cells stably transduced with IRE1-TurboID target constructs were treated with TM (5 μ g/mL) for 2 h before the addition of biotin (500 μ M) for 1 h. Biotinylated proteins were collected on streptavidinmagnetic beads for the subsequent identification and quantification by mass spectrometry (LC-MS/MS). (B) PCA plot showing the segregation of the identified interactomes in DMSO- or TM-treated samples between the control (con, V5-TurboID) and the IRE1 α /IRE1 β cellular models across the two PCA axes. Data points of con (green symbols), IRE1 α -TurboID (red symbols), and IRE1 β -TurboID (blue symbols); three biological

replicates are shown. Percentages correspond to the relative contribution of each axis to the overall variation in protein expression. (C) Venn diagram of 194 IRE1-interacting proteins shows unique and overlapping interactors of IRE1 α - and IRE1 β -TurboID fusion proteins in the presence of DMSO and TM. (D) Hierarchical clustering was performed with the top 250 overrepresented proteins in terms of change in significant LFQ intensity and enrichment compared to control, and the results are shown as a heatmap (distance is the Euclidean distance, and clustering algorithm using ward D). The fold changes were transformed to \log_{10} , and auto-scaling values were compared using one-way ANOVA with a p -value threshold of 0.01, with multiple comparisons corrected using statistical hypothesis testing (Tukey). (E) Volcano plot displays quantified protein interactors of IRE1 α compared to the control. The x-axis displays \log_2 fold change of enriched proteins. Blue dots show proteins that were at least 2-fold enriched, orange dots show further investigated proteins, and the red dot indicates IRE1 α . The y-axis displays \log_{10} p -value with the threshold set at $p < 0.05$. (F) STRING analysis of the IRE α interactors. All proteins were at least 2-fold upregulated in both IRE1 α vs. control as well as IRE1 α vs. IRE1 β . The colors show the Gene Ontology analysis results of proteins with ER localization (GO:0005783; orange), involved in the ER stress response (GO:0034976; green) and ER to Golgi vesicle-mediated transport (GO:0006888; blue).

3.3. IRE1 α Interacts with Proteins Involved in Vesicle Transport and Protein Stabilization

On the basis of the aforementioned GO terms (Figure S2D), our next focus was directed toward three main classifications: ER to Golgi vesicle-mediated transport, negative regulators of apoptosis (oncoproteins), and the ERAD pathway. We generated box plot graphs for each protein of interest, focusing first on proteins in contact with the ER, such as VAPA, or the nuclear membrane, such as emerin. Additionally, we focused on the classified oncoproteins and RISC complex members MTDH and SND1. While VAPA (Figure 3A) and emerin (Figure 3B) were enriched in both IRE1 α - and IRE1 β -containing protein complexes, MTDH (Figure 3C), SND1 (Figure 3D), and the AAA ATPase VCP (Figure 3E) were only enriched in IRE1 α -positive cells, suggesting differential regulation by interacting proteins of IRE1 α and IRE1 β . In contrast, the heat shock protein HSP90 showed a stronger interaction with IRE1 β (Figure 3F).

These interactions were confirmed through co-immunoprecipitation experiments using FLAG-hIRE1 α or an empty vector control (MOCK), both stably transduced in HMC-1.2^{IRE1 α -/-} cells, followed by treatments with the ER stressor TM or the solvent control DMSO. The immunoblot analyses confirmed interactions between FLAG-tagged IRE1 α and endogenous VAPA, Emerin, and MTDH but not with the MOCK control (Figure 3G). In order to validate the interaction between IRE1 α and VCP, we performed co-immunoprecipitation assays with FLAG-tagged hIRE1 α or GFP-tagged hVCP in HEK 293T cells. Consistently, we confirmed that VCP could be precipitated via GFP-specific antibodies (Figure 3H) and IRE1 α could be precipitated via FLAG-specific antibodies (Figure 3I). These results not only validated the TurboID analyses, but also revealed the diversity in the protein interactions of IRE1 α .

3.4. VCP Inhibition Stimulates UPR Activation and Enhancement of IRE1 α Expression

Based on the observed interaction of VCP with IRE1 α , we next investigated the consequences of VCP inhibition on IRE1 α expression and UPR activation. A previous study demonstrated that VCP inhibition causes the activation of the UPR [38]. Two VCP inhibitors, CB-5803 (Figure 4A) and NMS-873 (Figure S4A), were used to block the ATPase activity of VCP in HMC-1.2 cells. A significantly increased amount of IRE1 α and BIP was detectable after 18 h of VCP inhibition (Figure 4A,B), which also resulted in the detection of increased phosphorylation of IRE1 α at S724 (Figures 4A and S4A), suggesting the induction of ER stress by blockade of the ERAD mechanism. Additionally, *ERN1* (Figure 4C) and *XBPs* (Figure 4D) mRNA expression levels were increased by VCP inhibition together with *HSPA5* (Figure 4E) and *CHOP* mRNA (Figure 4F). The increased protein and mRNA levels suggest a cooperation between stress-mediated induction of transcription (and translation) as well as inhibitor-mediated blockade of homeostatic degradation.

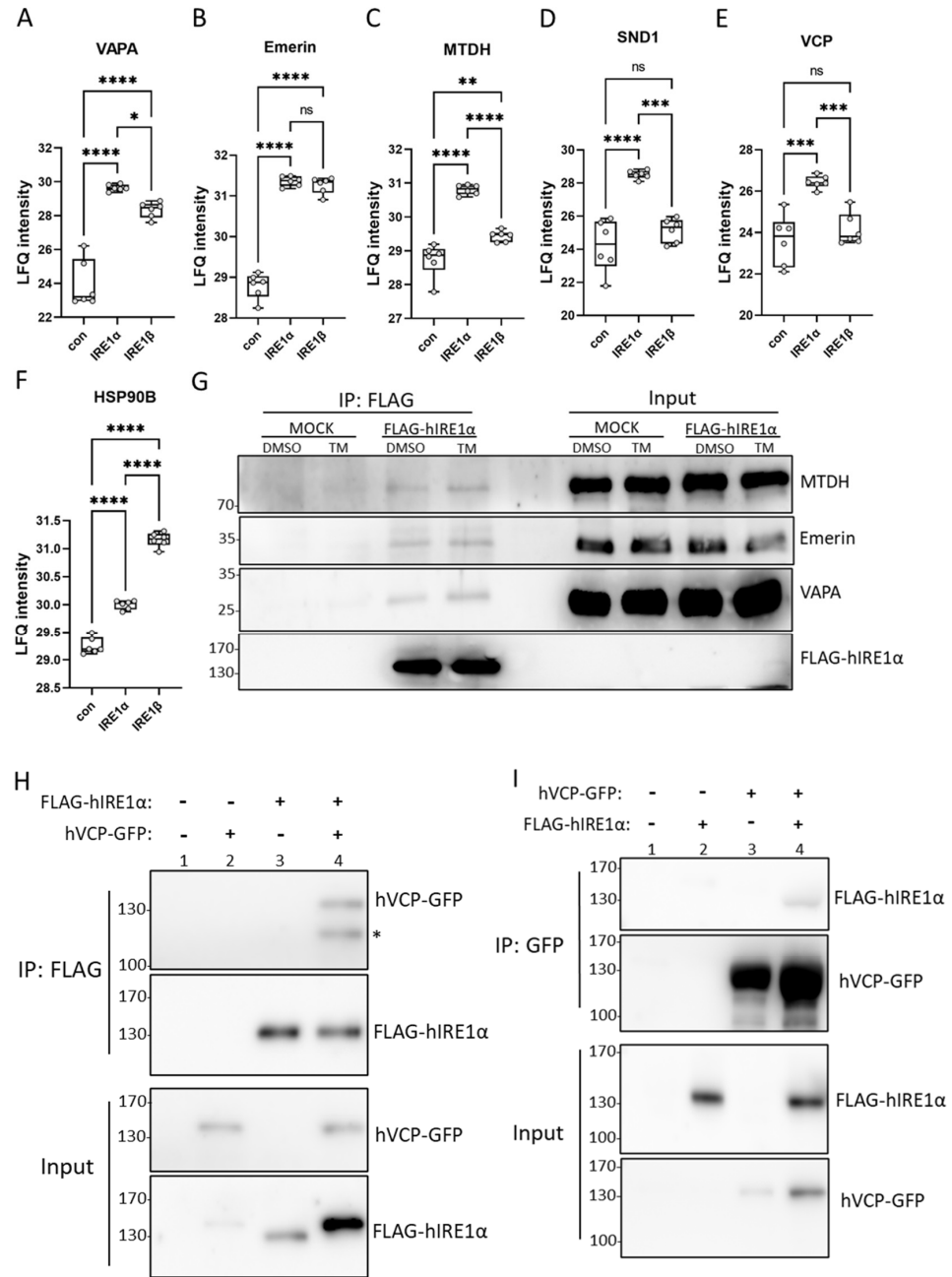


Figure 3. IRE1 α interacts with proteins involved in membrane contact sites and protein stabilization. (A–F) Boxplots depict LFQ values of the interactors detected by LC/MS TurboID: VAPA, emerlin, MTDH, SND1, VCP, and HSP90B, respectively. (G) HMC-1.2^{IRE1 α -/-} cells stably transduced with FLAG-tagged human IRE1 α or the empty vector control (MOCK) were treated with the solvent DMSO or TM (5 μ g/mL) for 3 h. IRE1 α was immunoprecipitated (IP) from cell lysates via an anti-FLAG antibody. Input and IP samples were immunoblotted for the detection of IRE1 α , MTDH, emerlin, and VAPA. (H,I) GFP-tagged VCP and FLAG-tagged IRE1 α were overexpressed in HEK293 cells. IRE1 α (α -FLAG) (H) and VCP (α -GFP) (I) were immunoprecipitated from lysates (Input) for further detection on immunoblots. (H) Top panel: notably, the band marked with an asterisk was not stably observed; bottom panel: this is the result of a consecutive detection, first with the α -GFP antibody and second with the α -FLAG antibody. hVCP-GFP is only slightly larger than FLAG-hIRE1 α (approximately 2 kDa) and it was more strongly expressed. (I) As can be seen in the bottom panel, the expression of hVCP-GFP was inhomogeneous, which, consequently, was also observed in the second panel from the top upon immunoprecipitation. Data shown as mean \pm SD. Significance levels are based on one-way ANOVA. * $p < 0.05$, ** $p < 0.01$, *** $p < 0.001$, **** $p < 0.0001$.

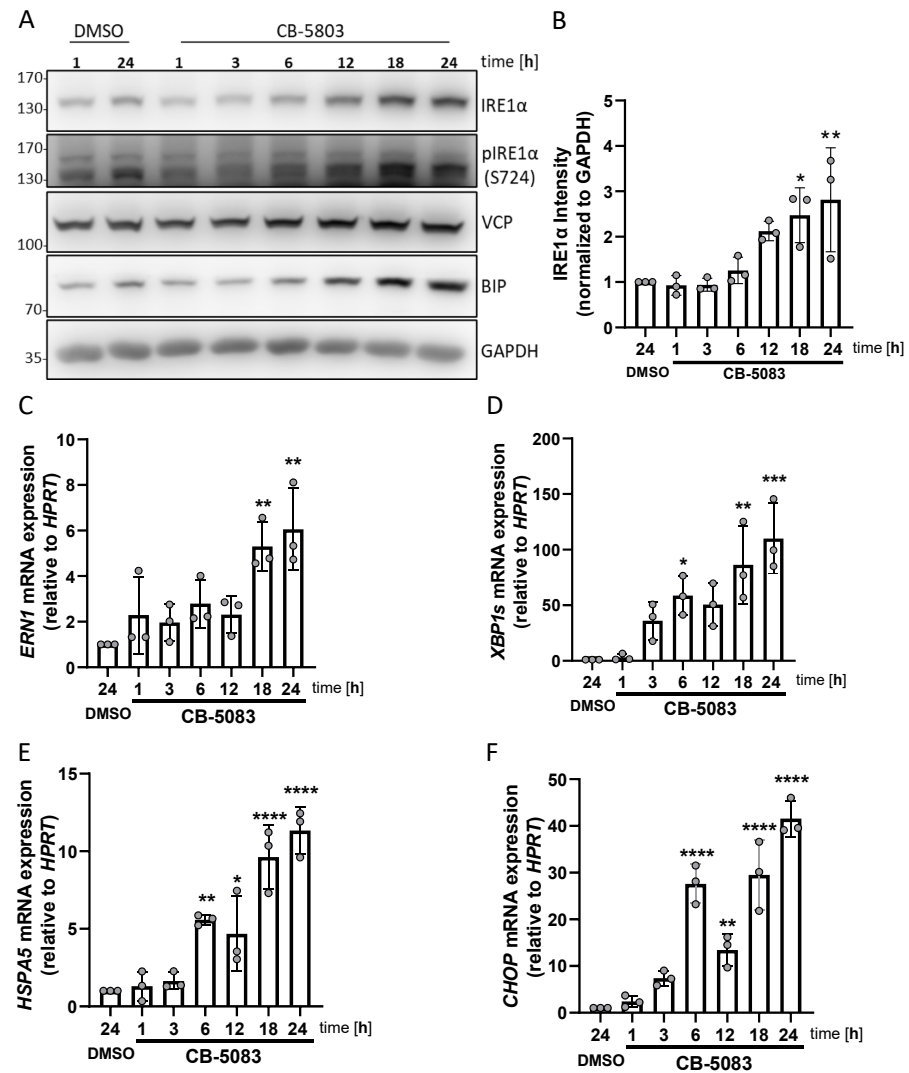


Figure 4. VCP inhibition stimulates UPR activation and IRE1α expression. (A) HMC-1.2 cells were treated with vehicle (DMSO) or 1 μM CB-5083 for the indicated time points. The phosphorylation of IRE1α (S724) and the expression of IRE1α, VCP, and BIP were detected by Western blotting. GAPDH served as the loading control. (B) Quantification (densitometry) of the data shown in (A) is the mean of three independent experiments. (C–F) HMC-1.2 cells were treated with vehicle (DMSO) or 1 μM CB-5083 for the indicated time points. *ERN1* (C), *XBP1s* (D), *HSPA5* (E), and *CHOP* (F) mRNA expression was evaluated by RT-qPCR and normalized to HPRT (n = 3). Data shown as mean ± SD. Significance levels are based on one-way ANOVA. * p < 0.05, ** p < 0.01, *** p < 0.001, **** p < 0.0001.

Interestingly, a similar activation of the UPR by VCP inhibition was observed in additional cancer cell lines, such as Jurkat and K562 cells, indicating a conserved mechanism across various cancer types (Supplementary Figure S4B,C). Collectively, these observations suggest that the inhibition of VCP in the MCL cell line HMC-1.2 induces ER stress and activates the UPR, particularly the IRE1α–XBP1s pathway, resulting in the increased expression of UPR target genes.

3.5. The Interaction between IRE1α, VCP, and MTDH Is Dependent on Ubiquitination

During ERAD, VCP associates with ubiquitin ligases located at the ER and extracts misfolded proteins from the ER [39]. To comprehensively understand the observed effects of VCP inhibition and the physical interaction between IRE1α and VCP, our investigation incorporated the interaction of IRE1α with MTDH, which is recognized as a type II ER transmembrane protein [40]. First, to analyze whether the interaction of IRE1α with VCP

or MTDH is dependent on ER stress, we treated HMC-1.2^{FLAG-IRE1α} cells with the pharmacological ER stress inducers TM or bortezomib (BZ). Second, to study if the interaction of IRE1α with VCP or MTDH is dependent on VCP activity or ubiquitination, we treated the cells for 3 h with the VCP inhibitor CB-5803 or the inhibitor of the E1 ubiquitin-activating enzyme MLN7243. Subsequently, we conducted co-immunoprecipitation assays using anti-FLAG antibody-coupled beads (to precipitate FLAG-hIRE1α) in order to determine the effects of these treatments on the IRE1α–VCP and IRE1α–MTDH interactions (Figure 5A–C). Interestingly, the results of our study indicated that the interaction between IRE1α and VCP or IRE1α and MTDH is mostly dependent on ubiquitination, as demonstrated by the significantly reduced interaction in cells exposed to the E1 inhibitor MLN7243 (Figure 5A–C). The impact of MLN7243 on global protein ubiquitination in the parental HMC-1.2 cells is shown in Figure S5B. In addition, we confirmed the ubiquitin-dependent interaction of endogenous IRE1α with VCP in the parental HMC-1.2 cells (Figure S3D). Moreover, the IRE1α variant IRE1α_{delta589-903} containing only Lys545 still interacted with VCP (Figure S3E). In addition, the kinase-inactive variant IRE1α KD (K599A) also interacted with hVCP-GFP, excluding a role of the kinase activity for this interaction (Figure S3E).

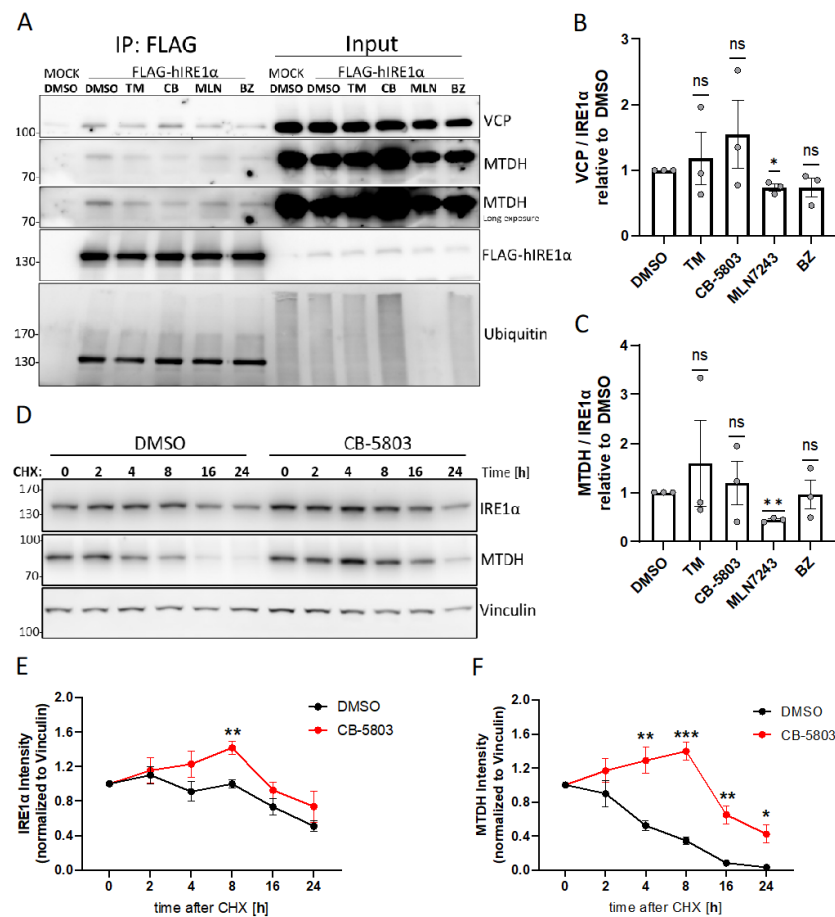


Figure 5. The interaction between IRE1α, VCP, and MTDH is dependent on ubiquitination. (A) HMC-1.2^{IRE1α-/-} cells stably transduced with FLAG-tagged human IRE1α or the empty vector control (MOCK) were treated as indicated with vehicle DMSO, 5 μg/mL TM, 1 μM CB-5803 (CB), 20 μM MLN7243 (MLN), or 10 nM bortezomib (BZ) for 3 h. Flag-tagged IRE1α was precipitated from lysates and analyzed together with the input on immunoblots for the detection of VCP, MTDH, IRE1α, and ubiquitin. Notably, the distinct bands seen on the left side of the ubiquitin panel are the IRE1α signal from the initial α-IRE1α detection prior to the incubation with the α-ubiquitin antibody. (B,C) Quantification (densitometry) of VCP (B) and MTDH (C) from blots in (A) is shown as the mean of three independent experiments. (D) Cycloheximide (CHX) chase assay in the presence of the

VCP inhibitor CB-5803 (1 μ M) or the solvent DMSO. CHX-treated HMC-1.2 cells were lysed at the indicated time points and IRE1 α and MTDH were detected by Western blotting. Vinculin served as the loading control. (E,F) Quantification (densitometry) of three independent experiments. IRE1 α (E) and MTDH (F) signals were normalized to the loading control and displayed values are relative to those in untreated cells. Error bars, s.e.m.; * $p < 0.05$, ** $p < 0.01$, *** $p < 0.001$, ns not-significant.

3.6. VCP Inhibition Stabilizes Expression of IRE1 α and MTDH

As shown above, VCP inhibition by CB-5803 resulted in the increased expression of IRE1 α and induction of ER stress (Figure 4A). We next analyzed the effect of pharmacological VCP inhibition on IRE1 α and MTDH protein stability. Therefore cycloheximide (CHX) chase assays were performed, wherein the HMC-1.2 cells were incubated with the translation inhibitor CHX in the presence or absence of the VCP inhibitors, CB-5803 or NMS-873. The subsequent immunoblot analyses showed a gradual decrease in IRE1 α expression over a 24 h period in DMSO-treated cells. In contrast to the DMSO-treated cells, in the presence of the VCP inhibitors, the half-life of IRE1 α was significantly prolonged (Figures 5D,E and S5A). Compared to IRE1 α , MTDH showed a distinct expression profile, with a rapid decrease already observed after 4 h. Similar to IRE1 α , the half-life of MTDH was significantly prolonged by the treatment with CB-5803 (Figures 5D,F and S5A). These results suggest that both IRE1 α [41] and MTDH are substrates for ERAD, with their stability directly affected by VCP activity.

3.7. IRE1 α Increases the Stability of MTDH Protein

Finally, we investigated if IRE1 α contributes to the stabilization of MTDH. The previous experiments suggested that the stability of both IRE1 α and MTDH is dependent on VCP activity. We compared CHX-treated parental HMC-1.2 with HMC-1.2^{IRE1 α -/-} cells to investigate whether the presence of IRE1 α affects the stability of MTDH. Indeed, the absence of IRE1 α in the HMC-1.2^{IRE1 α -/-} cells significantly reduced the stability of MTDH at an early time point (2 h) (Figure 6A,B). In conclusion, these data suggest an adaptive role of IRE1 α in supporting the stability of the ER membrane protein MTDH.

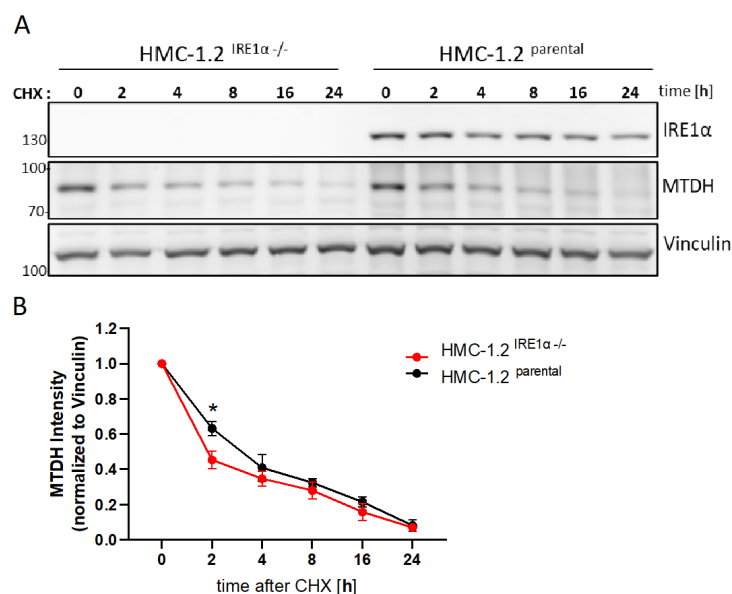


Figure 6. IRE1 α increases the protein stability of MTDH. (A) CHX chase assays were conducted in parental HMC-1.2 and IRE1 α -deficient cells. Cells were lysed at the indicated time points after CHX incubation and MTDH was detected by Western blotting. Vinculin served as the loading control. (B) Quantification (densitometry) of three independent experiments. MTDH signals were normalized to the loading control and displayed values are relative to those in untreated cells. Error bars, s.e.m.; * $p < 0.05$.

4. Discussion

MCL is known as the most aggressive form of SM. A key aspect of MCL, together with other types of cancer, is its enhanced translational activity and hence a susceptibility to an accumulation of misfolded proteins, resulting in constitutive activation of stress responses including the UPR. Suppressing the UPR has been identified as a potential strategy for cancer treatment [8,42]. Within this context, the role of IRE1 in modulating the balance between cellular survival and apoptosis under varying stress conditions is crucial but has not been fully elucidated for MCL.

Our previous work demonstrated that pharmacological inhibition of IRE1 as well as its forced activation could attenuate proliferation and increase apoptotic cell death of the MCL cell line HMC-1.2. Here, we aimed to identify new interactors that are involved in the regulation of IRE1 function. To reach a higher sensitivity compared to immunoprecipitation approaches, we applied the BioID technique, which allows for the detection of weak and transient protein interactions. In particular, we made use of the advanced BioID variant TurboID [43], which has the advantage of requiring only a short (1 h) incubation period with biotin, to modify/identify bait (IRE1)-interacting proteins. However, the biotinylation of indirect interactors or proximal proteins that do not interact directly are usually present and need to be accounted for [44].

Although we mainly concentrated on the analysis of IRE1 α -interacting proteins, we used this research work to identify IRE1 β interactors as well and to define the differences between the IRE1 α and IRE1 β isoforms.

IRE1 β has been reported to be uniquely expressed in epithelial cells lining mucosal surfaces [17]. There, it could negatively regulate IRE1 α signaling in response to ER stress [18]. However, the presence of endogenous IRE1 β protein was never confirmed due to the absence of specific antibodies. For the first time, we were able to detect the expression of IRE1 β (*ERN2*) mRNA in human MCL cell lines (HMC-1.1 and HMC-1.2), and other cancer cell lines. IRE1 β peptides were identified in a variety of MS data sets, including colorectal cancer tissues [45] as well as the NCI60 cell line panel [46]. Importantly, IRE1 β gene deletion strongly decreased the basal IRE1 β mRNA levels together with a reduction in *XBPIs* mRNA levels, suggesting the participation of IRE1 β in *XBPI* splicing and target gene expression.

The function of IRE1 α depends on its dimerization/oligomerization and phosphorylation state. These are affected by different factors that tune the balance between IRE1 α dimers and oligomers to determine the amplitude and kinetics of UPR signaling, for instance, the Sec61 core component of the translocon complex [47]. IRE1 α forms a dynamic multi-protein platform termed the UPRosome [48] that can contact other protein complexes and organelles. Several cytosolic inhibitors, positive modulators, and post-translational modifiers of IRE1 α have been identified. While Bax inhibitor-1 (TMBIM6) [49], fortilin [50], and BID [51] were identified as inhibitors, the BCL-2 family members BAX and BAK [52] can act as positive modulators. Moreover, it has been shown that the stability and activity of IRE1 α can be modified by post-translational modifications like phosphorylation [53] or ADP-ribosylation [54].

Our analysis confirmed previously described interactors of IRE1 α such as the chaperone HSP90 [55] and the translocon complex member Sec63 [47,56]. Moreover, several proteins involved in the ubiquitin-modification system were identified as IRE1-binding partners such as CHIP, ubiquitin D, USP14, and the UFM1-binding protein DDRGK1 [12,57].

We have additionally detected in our TurboID approach the E3 ligase UFL1 [58] as well as UBXN4, which connects IRE1 α to VCP and ERAD [59]. IRE1 α has been described as a target of the Sel1L-Hrd1 ERAD complex [41], which degrades IRE1 α under basal conditions in a BIP-dependent manner.

Importantly, we have identified the AAA ATPase VCP as a direct interactor of IRE1 α that affects IRE1 α expression and degradation. VCP is a crucial component of the ubiquitin-proteasome system that plays a central role in ERAD. Its functions are to pull out misfolded proteins from the ER lumen and membrane for degradation, to extract ubiquitylated

proteins from other membranes or cellular structures, and to segregate such proteins from interacting proteins to facilitate their degradation in the proteasome [60]. Interestingly, VCP is also involved in segregating transcription factors from chromatin and disassembling RNA–protein complexes [61]. The function of VCP is strongly dependent on its interaction with various cofactors, including ubiquitin adaptors, ubiquitin ligases, and deubiquitylating enzymes, to edit the ubiquitin chains on substrate proteins, thus determining their fate [60]. Active VCP is organized into a hexameric complex [39]; however, the technique used in our study does not allow us to differentiate between monomeric, dimeric, and hexameric VCP. Nevertheless, the effects of pharmacological VCP inhibitors point to the importance of active, hexameric VCP.

Due to VCP's central role in ERAD and the ability to induce irreversible proteotoxic stress through VCP inhibition, several VCP inhibitors are being tested in clinical trials [62]. The first-in-class VCP inhibitor CB-5083 has been demonstrated to exert cytotoxicity *in vitro* against canine lymphoma [63]. Interestingly, dogs commonly present with mast cell tumors in the skin [64], suggesting the efficacy of VCP inhibitors in such tumors as well. The survival and proliferation of cancer cells is strongly dependent on an adaptive UPR. This pro-survival mechanism can be switched to the pro-apoptotic, terminal UPR by forcing ER stress. This could be achieved by the inhibition of VCP, the main executor of ERAD, or the inhibition of the most conserved ER stress sensor IRE1 α , which is mainly involved in protein homeostasis. Therefore, the combined inhibition of VCP and IRE1 α could be more effective, allowing for the use of lower inhibitor concentrations and potentially attenuating side effects.

Mast cells release preformed mediators from so-called secretory lysosomes. We have identified the Vesicle-Associated Membrane Protein-Associated Protein A (VAPA), which plays a crucial role in vesicle trafficking, membrane fusion, protein complex assembly, and cell motility, as an IRE1 interactor. ER-resident VAPA forms ER–endosome contact sites via interactions with Oxysterol-Binding Protein 1 (OSBP) to mediate its lipid transfer function [65]. In addition, VAPA is also involved in autophagy [66] and ER-phagy, which are essential mechanisms in the UPR [67]. It has been shown in yeast that the soluble ER-phagy receptor Epr1 is upregulated via IRE1 signaling [68]. The selective autophagy receptor optineurin interacts with IRE1 α , and optineurin deficiency amplifies IRE1 α levels during ER stress [69]. Here, we described for the first time a direct interaction between VAPA and IRE1 α in an MCL model system. Whether VAPA is involved in MC granule formation or autophagy needs further investigation. Interestingly, IRE1 also interacted with the nuclear membrane protein Emerin, suggesting that IRE1 also contacts the nuclear membrane. However, it has been reported that Emerin dissociates from the nuclear envelope during ER stress [70] and thus, IRE1 might interact with cytosolic emerin.

The interaction of MTDH with IRE1 α and its destabilization by VCP offers an interesting view on tumor control by functionally interacting MTDH, IRE1 α , and VCP. MTDH depletion or pharmacological inhibition disrupts the interaction with staphylococcal nuclease domain-containing 1 (SND1), which is required to sustain breast cancer progression in established tumors [15]. Pharmacological disruption of the MTDH–SND1 complex enhances tumor antigen presentation and synergizes with anti-PD-1 therapy in metastatic breast cancer [71]. Since we showed that VCP activity controls basal MTDH expression levels, the careful use of pharmacological VCP activators might attenuate the progression of breast cancer. Cytoplasmic MTDH has been shown to provide a survival advantage under conditions of stress by acting as an RNA-binding protein [15]. As mentioned before, SND1, which acts as a nuclease in the RNA-induced silencing complex (RISC) facilitating RNAi-mediated gene silencing, is an MTDH-interacting protein. Co-immunoprecipitation and co-localization studies confirmed that MTDH is also a component of the RISC, and both MTDH and SND1 are required for optimum RISC activity. Increased RISC activity, conferred by MTDH or SND1, resulted in increased degradation of tumor suppressor mRNAs that are targets of oncomiRs [72]. We have identified MTDH and SND1 as IRE1 α interactors and showed that the stability of MTDH was increased by VCP inhibition, suggesting that

MTDH is a target of the VCP-ERAD machinery. Its role as an RNA-binding protein and as a member of the RISC could have a potential impact on IRE1 α -processed RNAs and needs further investigations.

An overview on the mentioned/analyzed factors and their potential functions on the basis of the relevant GO terms is shown in Supplementary Table S1.

5. Conclusions

IRE1 α is a central regulator of the UPR, which is required, amongst other processes, for proteostasis in proliferating cancer cells. Using the technique of TurboID, we identified novel and verified already known IRE1 α -interacting proteins in the KIT^{D816V}-driven MCL cell line HMC-1.2. In particular, the interaction of IRE1 α with VCP, a main constituent of the ERAD pathway, suggests a close functional interaction between the detection of misfolded proteins by IRE1 α and the removal of such proteins from the ER by VCP. The development and use of pharmacological activators and inhibitors of IRE1 α as well as VCP will allow for the careful titration of proteostasis and thus the optimization of the adaptive UPR or maximization of the terminal UPR for cancer therapy. Further identification and analyses of IRE1 α -interacting proteins will enable the organ- and cell type-specific elimination of neoplastic cells.

6. Limitations of the Study

The study presented in this publication was mainly performed in the MCL cell line HMC-1.2, which expresses KIT^{V560G,D816V}. Working with this cell line allowed us to conduct the analyses presented (TurboID-based identification of IRE1 α interaction partners and verification by immunoprecipitation). The verification of the obtained data using primary leukemia cells from MCL patients would strengthen the conclusions of our study; however, due to limitations in obtaining sufficient cell numbers, this was not possible. Moreover, the biochemical verification of the differences/similarities between the IRE1 α and IRE1 β interaction partners identified in our BioID approach would have been preferable. Due to the unavailability of a suitable anti-IRE1 β antibody, a confirmation of the endogenous levels was not possible.

Supplementary Materials: The following supporting information can be downloaded at: <https://www.mdpi.com/article/10.3390/cells13090747/s1>, Figure S1: UPR activation in parental HMC-1.2 and IRE1 α - or IRE1 β -deficient cell lines; Figure S2: Characterization of the IRE1 α -TurboID fusion protein; Figure S3: IRE1 α interactions in HMC-1.2 cells; Figure S4: VCP inhibition stimulates UPR activation and IRE1 α expression/stabilization; Figure S5: VCP inhibition by NMS-873 stabilizes IRE1 α and MTDH; Table S1: Overview on the mentioned/analyzed factors and their potential functions on the basis of the relevant GO terms. Ratios and *p*-values of the individual comparisons.

Author Contributions: N.A.: data curation, formal analysis, investigation, methodology, project administration, software, validation, visualization, writing—original draft, writing—review and editing; C.P.: data curation, formal analysis, software, writing—review and editing; T.W.: conceptualization, investigation, methodology, supervision, validation, visualization, writing—original draft, writing—review and editing; M.H.: conceptualization, funding acquisition, project administration, resources, supervision, visualization, writing—original draft, writing—review and editing. All authors have read and agreed to the published version of the manuscript.

Funding: This research was funded by grants from the German-Israeli Foundation for Scientific Research and Development (Grant No. I-1471-414.13/2018) to M.H., and the START Program of the Medical Faculty of the RWTH Aachen University (T.W., 691517).

Institutional Review Board Statement: The study did not require ethical approval.

Informed Consent Statement: The study did not involve primary human material.

Data Availability Statement: The mass spectrometry proteomics data have been deposited to the ProteomeXchange Consortium via the PRIDE [73] partner repository with the dataset identifier PXD047343.

Acknowledgments: The authors acknowledge the expert technical assistance of K. Maschke-Neuß as well as the contribution of M. Griebel. The valuable contribution of Boaz Tirosh (incumbent of the David Eisenberg Chair in Pharmacy) in funding acquisition and manuscript review is acknowledged and appreciated.

Conflicts of Interest: The authors declare no conflicts of interests.

References

- Huber, M.; Cato, A.C.B.; Ainooson, G.K.; Freichel, M.; Tsvilovskyy, V.; Jessberger, R.; Riedlinger, E.; Sommerhoff, C.P.; Bischoff, S.C. Regulation of the pleiotropic effects of tissue-resident mast cells. *J. Allergy Clin. Immun.* **2019**, *144*, S31–S45. [[CrossRef](#)] [[PubMed](#)]
- Metcalfe, D.D. Mast cells and mastocytosis. *Blood* **2008**, *112*, 946–956. [[CrossRef](#)] [[PubMed](#)]
- Ustun, C.; Arock, M.; Kluijn-Nelemans, H.C.; Reiter, A.; Sperr, W.R.; George, T.; Horny, H.-P.; Hartmann, K.; Sotlar, K.; Damaj, G.; et al. Advanced systemic mastocytosis: From molecular and genetic progress to clinical practice. *Haematologica* **2016**, *101*, 1133–1143. [[CrossRef](#)] [[PubMed](#)]
- Akin, C.; Kirshenbaum, A.S.; Semere, T.; Worobec, A.S.; Scott, L.M.; Metcalfe, D.D. Analysis of the surface expression of c-kit and occurrence of the c-kit Asp816Val activating mutation in T cells, B cells, and myelomonocytic cells in patients with mastocytosis. *Exp. Hematol.* **2000**, *28*, 140–147. [[CrossRef](#)] [[PubMed](#)]
- Fritsche-Polanz, R.; Jordan, J.; Feix, A.; Sperr, W.R.; Sunder-Plassmann, G.; Valent, P.; Födinger, M. Mutation analysis of C-KIT in patients with myelodysplastic syndromes without mastocytosis and cases of systemic mastocytosis. *Br. J. Haematol.* **2001**, *113*, 357–364. [[CrossRef](#)] [[PubMed](#)]
- Longley, B.J.; Metcalfe, D.D.; Tharp, M.; Wang, X.; Tyrrell, L.; Lu, S.; Heitjan, D.; Ma, Y. Activating and dominant inactivating c-KIT catalytic domain mutations in distinct clinical forms of human mastocytosis. *Proc. Natl. Acad. Sci. USA* **1999**, *96*, 1609–1614. [[CrossRef](#)] [[PubMed](#)]
- Gleixner, K.V.; Peter, B.; Blatt, K.; Suppan, V.; Reiter, A.; Radia, D.; Hadzijušufovic, E.; Valent, P.; Gleixner, K.V. Synergistic growth-inhibitory effects of ponatinib and midostaurin (PKC412) on neoplastic mast cells carrying KIT D816V. *Haematologica* **2013**, *98*, 1450–1457. [[CrossRef](#)] [[PubMed](#)]
- Wilhelm, T.; Bick, F.; Peters, K.; Mohta, V.; Tirosh, B.; Patterson, J.B.; Kharabi-Masouleh, B.; Huber, M. Inflection of proteotoxic stresses by impairment of the unfolded protein response or proteasomal inhibition as a therapeutic strategy for mast cell leukemia. *Oncotarget* **2017**, *9*, 2984–3000. [[CrossRef](#)] [[PubMed](#)]
- Hetz, C.; Chevet, E.; Oakes, S.A. Proteostasis control by the unfolded protein response. *Nat. Cell Biol.* **2015**, *17*, 829–838. [[CrossRef](#)]
- Calfon, M.; Zeng, H.; Urano, F.; Till, J.H.; Hubbard, S.R.; Harding, H.P.; Clark, S.G.; Ron, D. IRE1 couples endoplasmic reticulum load to secretory capacity by processing the XBP-1 mRNA. *Nature* **2002**, *415*, 92–96. [[CrossRef](#)]
- Yamamoto, K.; Sato, T.; Matsui, T.; Sato, M.; Okada, T.; Yoshida, H.; Harada, A.; Mori, K. Transcriptional Induction of Mammalian ER Quality Control Proteins Is Mediated by Single or Combined Action of ATF6 α and XBP1. *Dev. Cell* **2007**, *13*, 365–376. [[CrossRef](#)] [[PubMed](#)]
- Christianson, J.C.; Jarosch, E.; Sommer, T. Mechanisms of substrate processing during ER-associated protein degradation. *Nat. Rev. Mol. Cell Biol.* **2023**, *24*, 777–796. [[CrossRef](#)]
- Braxton, J.R.; Southworth, D.R. Structural insights of the p97/VCP AAA+ ATPase: How adapter interactions coordinate diverse cellular functionality. *J. Biol. Chem.* **2023**, *299*, 105182. [[CrossRef](#)] [[PubMed](#)]
- Emdad, L.; Das, S.K.; Dasgupta, S.; Hu, B.; Sarkar, D.; Fisher, P.B. Chapter Three AEG-1/MTDH/LYRIC Signaling Pathways, Downstream Genes, Interacting Proteins, and Regulation of Tumor Angiogenesis. *Adv. Cancer Res.* **2013**, *120*, 75–111. [[CrossRef](#)] [[PubMed](#)]
- Meng, X.; Zhu, D.; Yang, S.; Wang, X.; Xiong, Z.; Zhang, Y.; Brachova, P.; Leslie, K.K. Cytoplasmic Metadherin (MTDH) Provides Survival Advantage under Conditions of Stress by Acting as RNA-binding Protein*. *J. Biol. Chem.* **2012**, *287*, 4485–4491. [[CrossRef](#)] [[PubMed](#)]
- Hetz, C.; Zhang, K.; Kaufman, R.J. Mechanisms, regulation and functions of the unfolded protein response. *Nat. Rev. Mol. Cell Biol.* **2020**, *21*, 421–438. [[CrossRef](#)] [[PubMed](#)]
- Martino, M.B.; Jones, L.; Brighton, B.; Ehre, C.; Abdulah, L.; Davis, C.W.; Ron, D.; O’Neal, W.K.; Ribeiro, C.M.P. The ER stress transducer IRE1 β is required for airway epithelial mucin production. *Mucosal Immunol.* **2013**, *6*, 639–654. [[CrossRef](#)] [[PubMed](#)]
- Grey, M.J.; Cloots, E.; Simpson, M.S.; LeDuc, N.; Serebrenik, Y.V.; Luca, H.D.; Sutter, D.D.; Luong, P.; Thiagarajah, J.R.; Paton, A.W.; et al. IRE1 β negatively regulates IRE1 α signaling in response to endoplasmic reticulum stress. *J Cell Biol.* **2020**, *219*, e201904048. [[CrossRef](#)]
- Lhomond, S.; Avril, T.; Dejeans, N.; Voutetakis, K.; Doultinos, D.; McMahon, M.; Pineau, R.; Obacz, J.; Papadodima, O.; Jouan, F.; et al. Dual IRE 1 RNase functions dictate glioblastoma development. *EMBO Mol. Med.* **2018**, *10*, e7929. [[CrossRef](#)] [[PubMed](#)]
- Sun, H.; Lin, D.-C.; Guo, X.; Masouleh, B.K.; Gery, S.; Cao, Q.; Alkan, S.; Ikezoe, T.; Akiba, C.; Paquette, R.; et al. Inhibition of IRE1 α -driven pro-survival pathways is a promising therapeutic application in acute myeloid leukemia. *Oncotarget* **2016**, *7*, 18736–18749. [[CrossRef](#)]

21. Zhao, N.; Cao, J.; Xu, L.; Tang, Q.; Dobrolecki, L.E.; Lv, X.; Talukdar, M.; Lu, Y.; Wang, X.; Hu, D.Z.; et al. Pharmacological targeting of MYC-regulated IRE1/XBP1 pathway suppresses MYC-driven breast cancer. *J. Clin. Investig.* **2018**, *128*, 1283–1299. [[CrossRef](#)]
22. Raymundo, D.P.; Doultisinos, D.; Guillory, X.; Carlesso, A.; Eriksson, L.A.; Chevet, E. Pharmacological Targeting of IRE1 in Cancer. *Trends Cancer* **2020**, *6*, 1018–1030. [[CrossRef](#)]
23. Butterfield, J.H.; Weiler, D.; Dewald, G.; Gleich, G.J. Establishment of an immature mast cell line from a patient with mast cell leukemia. *Leukemia Res.* **1988**, *12*, 345–355. [[CrossRef](#)] [[PubMed](#)]
24. Volmer, R.; van der Ploeg, K.; Ron, D. Membrane lipid saturation activates endoplasmic reticulum unfolded protein response transducers through their transmembrane domains. *Proc. Natl. Acad. Sci. USA* **2013**, *110*, 4628–4633. [[CrossRef](#)]
25. Lipson, K.L.; Ghosh, R.; Urano, F. The Role of IRE1 α in the Degradation of Insulin mRNA in Pancreatic β -Cells. *PLoS ONE* **2008**, *3*, e1648. [[CrossRef](#)]
26. Morgenstern, J.P.; Land, H. Advanced mammalian gene transfer: High titre retroviral vectors with multiple drug selection markers and a complementary helper-free packaging cell line. *Nucleic Acids Res.* **1990**, *18*, 3587–3596. [[CrossRef](#)] [[PubMed](#)]
27. Branon, T.C.; Bosch, J.A.; Sanchez, A.D.; Udeshi, N.D.; Svinkina, T.; Carr, S.A.; Feldman, J.L.; Perrimon, N.; Ting, A.Y. Efficient proximity labeling in living cells and organisms with TurboID. *Nat. Biotechnol.* **2018**, *36*, 880–887. [[CrossRef](#)] [[PubMed](#)]
28. Stewart, S.A.; Dykxhoorn, D.M.; Palliser, D.; Mizuno, H.; Yu, E.Y.; An, D.S.; Sabatini, D.M.; Chen, I.S.Y.; Hahn, W.C.; Sharp, P.A.; et al. Lentivirus-delivered stable gene silencing by RNAi in primary cells. *RNA* **2003**, *9*, 493–501. [[CrossRef](#)]
29. Ran, F.A.; Hsu, P.D.; Wright, J.; Agarwala, V.; Scott, D.A.; Zhang, F. Genome engineering using the CRISPR-Cas9 system. *Nat. Protoc.* **2013**, *8*, 2281–2308. [[CrossRef](#)]
30. Tresse, E.; Salomons, F.A.; Vesa, J.; Bott, L.C.; Kimonis, V.; Yao, T.-P.; Dantuma, N.P.; Taylor, J.P. VCP/p97 is essential for maturation of ubiquitin-containing autophagosomes and this function is impaired by mutations that cause IBMPFD. *Autophagy* **2010**, *6*, 217–227. [[CrossRef](#)]
31. Iwawaki, T.; Hosoda, A.; Okuda, T.; Kamigori, Y.; Nomura-Furuwatari, C.; Kimata, Y.; Tsuru, A.; Kohno, K. Translational control by the ER transmembrane kinase/ribonuclease IRE1 under ER stress. *Nat. Cell Biol.* **2001**, *3*, 158–164. [[CrossRef](#)]
32. Pfaffl, M.W. A new mathematical model for relative quantification in real-time RT-PCR. *Nucleic Acids Res.* **2001**, *29*, e45. [[CrossRef](#)] [[PubMed](#)]
33. Holzer, G.; Magistris, P.D.; Gramminger, C.; Sachdev, R.; Magalska, A.; Schooley, A.; Scheufen, A.; Lennartz, B.; Tatarek-Nossol, M.; Lue, H.; et al. The nucleoporin Nup50 activates the Ran guanine nucleotide exchange factor RCC1 to promote NPC assembly at the end of mitosis. *EMBO J.* **2021**, *40*, e108788. [[CrossRef](#)] [[PubMed](#)]
34. Tyanova, S.; Temu, T.; Cox, J. The MaxQuant computational platform for mass spectrometry-based shotgun proteomics. *Nat. Protoc.* **2016**, *11*, 2301–2319. [[CrossRef](#)] [[PubMed](#)]
35. Tyanova, S.; Temu, T.; Sinitcyn, P.; Carlson, A.; Hein, M.Y.; Geiger, T.; Mann, M.; Cox, J. The Perseus computational platform for comprehensive analysis of (prote)omics data. *Nat. Methods* **2016**, *13*, 731–740. [[CrossRef](#)] [[PubMed](#)]
36. Nolte, H.; MacVicar, T.D.; Tellkamp, F.; Krüger, M. Instant Clue: A Software Suite for Interactive Data Visualization and Analysis. *Sci. Rep.* **2018**, *8*, 12648. [[CrossRef](#)]
37. Urano, F.; Wang, X.; Bertolotti, A.; Zhang, Y.; Chung, P.; Harding, H.P.; Ron, D. Coupling of Stress in the ER to Activation of JNK Protein Kinases by Transmembrane Protein Kinase IRE1. *Science* **2000**, *287*, 664–666. [[CrossRef](#)] [[PubMed](#)]
38. Anderson, D.J.; Le Moigne, R.; Djakovic, S.; Kumar, B.; Rice, J.; Wong, S.; Wang, J.; Yao, B.; Valle, E.; Kiss von Soly, S.; et al. Targeting the AAA ATPase p97 as an Approach to Treat Cancer through Disruption of Protein Homeostasis. *Cancer Cell* **2015**, *28*, 653–665. [[CrossRef](#)]
39. Meyer, H.; Bug, M.; Bremer, S. Emerging functions of the VCP/p97 AAA-ATPase in the ubiquitin system. *Nat. Cell Biol.* **2012**, *14*, 117–123. [[CrossRef](#)]
40. Brown, D.M.; Ruoslahti, E. Metadherin, a cell surface protein in breast tumors that mediates lung metastasis. *Cancer Cell* **2004**, *5*, 365–374. [[CrossRef](#)]
41. Sun, S.; Shi, G.; Sha, H.; Ji, Y.; Han, X.; Shu, X.; Ma, H.; Inoue, T.; Gao, B.; Kim, H.; et al. IRE1 α is an endogenous substrate of endoplasmic-reticulum-associated degradation. *Nat. Cell Biol.* **2015**, *17*, 1546–1555. [[CrossRef](#)] [[PubMed](#)]
42. Hetz, C.; Axten, J.M.; Patterson, J.B. Pharmacological targeting of the unfolded protein response for disease intervention. *Nat. Chem. Biol.* **2019**, *15*, 764–775. [[CrossRef](#)] [[PubMed](#)]
43. May, D.G.; Scott, K.L.; Campos, A.R.; Roux, K.J. Comparative Application of BioID and TurboID for Protein-Proximity Biotinylation. *Cells* **2020**, *9*, 1070. [[CrossRef](#)] [[PubMed](#)]
44. Sears, R.M.; May, D.G.; Roux, K.J. Enzyme-Mediated Ligation Methods. *Methods Mol. Biol.* **2019**, *2012*, 299–313. [[CrossRef](#)] [[PubMed](#)]
45. Kume, H.; Muraoka, S.; Kuga, T.; Adachi, J.; Narumi, R.; Watanabe, S.; Kuwano, M.; Kodera, Y.; Matsushita, K.; Fukuoka, J.; et al. Discovery of Colorectal Cancer Biomarker Candidates by Membrane Proteomic Analysis and Subsequent Verification using Selected Reaction Monitoring (SRM) and Tissue Microarray (TMA) Analysis*. *Mol. Cell. Proteom.* **2014**, *13*, 1471–1484. [[CrossRef](#)] [[PubMed](#)]
46. Gholami, A.M.; Hahne, H.; Wu, Z.; Auer, F.J.; Meng, C.; Wilhelm, M.; Kuster, B. Global Proteome Analysis of the NCI-60 Cell Line Panel. *Cell Rep.* **2013**, *4*, 609–620. [[CrossRef](#)]

47. Sundaram, A.; Plumb, R.; Appathurai, S.; Mariappan, M. The Sec61 translocon limits IRE1 α signaling during the unfolded protein response. *eLife* **2017**, *6*, e27187. [[CrossRef](#)]
48. Hetz, C.; Glimcher, L.H. Fine-Tuning of the Unfolded Protein Response: Assembling the IRE1 α Interactome. *Mol. Cell* **2009**, *35*, 551–561. [[CrossRef](#)] [[PubMed](#)]
49. Lisbona, F.; Rojas-Rivera, D.; Thielen, P.; Zamorano, S.; Todd, D.; Martinon, F.; Glavic, A.; Kress, C.; Lin, J.H.; Walter, P.; et al. BAX Inhibitor-1 Is a Negative Regulator of the ER Stress Sensor IRE1 α . *Mol. Cell* **2009**, *33*, 679–691. [[CrossRef](#)]
50. Pinkaew, D.; Chattopadhyay, A.; King, M.D.; Chunhacha, P.; Liu, Z.; Stevenson, H.L.; Chen, Y.; Sinthujaroen, P.; McDougal, O.M.; Fujise, K. Fortilin binds IRE1 α and prevents ER stress from signaling apoptotic cell death. *Nat. Commun.* **2017**, *8*, 18. [[CrossRef](#)]
51. Bashir, S.; Banday, M.; Qadri, O.; Pal, D.; Bashir, A.; Hilal, N.; Altaf, M.; Fazili, K.M. The Bcl-2 family protein bid interacts with the ER stress sensor IRE1 to differentially modulate its RNase activity. *FEBS Lett.* **2023**, *597*, 962–974. [[CrossRef](#)] [[PubMed](#)]
52. Hetz, C.; Bernasconi, P.; Fisher, J.; Lee, A.-H.; Bassik, M.C.; Antonsson, B.; Brandt, G.S.; Iwakoshi, N.N.; Schinzel, A.; Glimcher, L.H.; et al. Proapoptotic BAX and BAK Modulate the Unfolded Protein Response by a Direct Interaction with IRE1 α . *Science* **2006**, *312*, 572–576. [[CrossRef](#)]
53. Mao, T.; Shao, M.; Qiu, Y.; Huang, J.; Zhang, Y.; Song, B.; Wang, Q.; Jiang, L.; Liu, Y.; Han, J.-D.; et al. PKA phosphorylation couples hepatic inositol-requiring enzyme 1 α to glucagon signaling in glucose metabolism. *Proc. Natl. Acad. Sci. USA* **2011**, *108*, 15852–15857. [[CrossRef](#)] [[PubMed](#)]
54. Jwa, M.; Chang, P. PARP16 is a tail-anchored endoplasmic reticulum protein required for the PERK- and IRE1 α -mediated unfolded protein response. *Nat. Cell Biol.* **2012**, *14*, 1223–1230. [[CrossRef](#)]
55. Marcu, M.G.; Doyle, M.; Bertolotti, A.; Ron, D.; Hendershot, L.; Neckers, L. Heat Shock Protein 90 Modulates the Unfolded Protein Response by Stabilizing IRE1 α . *Mol. Cell Biol.* **2002**, *22*, 8506–8513. [[CrossRef](#)]
56. Plumb, R.; Zhang, Z.-R.; Appathurai, S.; Mariappan, M. A functional link between the co-translational protein translocation pathway and the UPR. *eLife* **2015**, *4*, e07426. [[CrossRef](#)] [[PubMed](#)]
57. Urra, H.; Pihán, P.; Hetz, C. The UPORosome—Decoding novel biological outputs of IRE1 α function. *J. Cell Sci.* **2020**, *133*, jcs218107. [[CrossRef](#)]
58. Peter, J.J.; Magnussen, H.M.; DaRosa, P.A.; Millrine, D.; Matthews, S.P.; Lamoliatte, F.; Sundaramoorthy, R.; Kopito, R.R.; Kulathu, Y. A non-canonical scaffold-type E3 ligase complex mediates protein UFMylation. *EMBO J.* **2022**, *41*, e111015. [[CrossRef](#)]
59. Liang, J.; Yin, C.; Doong, H.; Fang, S.; Peterhoff, C.; Nixon, R.A.; Monteiro, M.J. Characterization of erasin (UBXD2): A new ER protein that promotes ER-associated protein degradation. *J. Cell Sci.* **2006**, *119*, 4011–4024. [[CrossRef](#)]
60. Meyer, H.; Weihl, C.C. The VCP/p97 system at a glance: Connecting cellular function to disease pathogenesis. *J. Cell Sci.* **2014**, *127*, 3877–3883. [[CrossRef](#)]
61. Zhou, H.-L.; Geng, C.; Luo, G.; Lou, H. The p97-UBXD8 complex destabilizes mRNA by promoting release of ubiquitinated HuR from mRNP. *Genes Dev.* **2013**, *27*, 1046–1058. [[CrossRef](#)] [[PubMed](#)]
62. Kilgas, S.; Ramadan, K. Inhibitors of the ATPase p97/VCP: From basic research to clinical applications. *Cell Chem. Biol.* **2023**, *30*, 3–21. [[CrossRef](#)] [[PubMed](#)]
63. Gareau, A.; Rico, C.; Boerboom, D.; Nadeau, M.-E. In vitro efficacy of a first-generation valosin-containing protein inhibitor (CB-5083) against canine lymphoma. *Vet. Comp. Oncol.* **2018**, *16*, 311–317. [[CrossRef](#)] [[PubMed](#)]
64. Willmann, M.; Yuzbasiyan-Gurkan, V.; Marconato, L.; Dacasto, M.; Hadzizijufovic, E.; Hermine, O.; Sadovnik, I.; Gamperl, S.; Schneeweiss-Gleixner, M.; Gleixner, K.V.; et al. Proposed Diagnostic Criteria and Classification of Canine Mast Cell Neoplasms: A Consensus Proposal. *Front. Vet. Sci.* **2021**, *8*, 755258. [[CrossRef](#)] [[PubMed](#)]
65. Mattia, T.D.; Martinet, A.; Ikhlef, S.; McEwen, A.G.; Nominé, Y.; Wendling, C.; Poussin-Courmontagne, P.; Voilquin, L.; Eberling, P.; Ruffenach, F.; et al. FFAT motif phosphorylation controls formation and lipid transfer function of inter-organelle contacts. *EMBO J.* **2020**, *39*, e104369. [[CrossRef](#)] [[PubMed](#)]
66. Zhao, Y.G.; Liu, N.; Miao, G.; Chen, Y.; Zhao, H.; Zhang, H. The ER Contact Proteins VAPA/B Interact with Multiple Autophagy Proteins to Modulate Autophagosome Biogenesis. *Curr. Biol.* **2018**, *28*, 1234–1245.e4. [[CrossRef](#)] [[PubMed](#)]
67. Senft, D.; Ronai, Z.A. UPR, autophagy, and mitochondria crosstalk underlies the ER stress response. *Trends Biochem. Sci.* **2015**, *40*, 141–148. [[CrossRef](#)]
68. Zhao, D.; Zou, C.-X.; Liu, X.-M.; Jiang, Z.-D.; Yu, Z.-Q.; Suo, F.; Du, T.-Y.; Dong, M.-Q.; He, W.; Du, L.-L. A UPR-Induced Soluble ER-Phagy Receptor Acts with VAPs to Confer ER Stress Resistance. *Mol. Cell* **2020**, *79*, 963–977.e3. [[CrossRef](#)]
69. Tschurtschenthaler, M.; Adolph, T.E.; Ashcroft, J.W.; Niederreiter, L.; Bharti, R.; Saveljeva, S.; Bhattacharyya, J.; Flak, M.B.; Shih, D.Q.; Fuhler, G.M.; et al. Defective ATG16L1-mediated removal of IRE1 α drives Crohn’s disease-like ileitis. *J. Exp. Med.* **2017**, *214*, 401–422. [[CrossRef](#)]
70. Buchwalter, A.; Schulte, R.; Tsai, H.; Capitanio, J.; Hetzer, M. Selective clearance of the inner nuclear membrane protein emerlin by vesicular transport during ER stress. *eLife* **2019**, *8*, e49796. [[CrossRef](#)]
71. Shen, M.; Smith, H.A.; Wei, Y.; Jiang, Y.-Z.; Zhao, S.; Wang, N.; Rowicki, M.; Tang, Y.; Hang, X.; Wu, S.; et al. Pharmacological disruption of the MTDH-SND1 complex enhances tumor antigen presentation and synergizes with anti-PD-1 therapy in metastatic breast cancer. *Nat. Cancer* **2022**, *3*, 60–74. [[CrossRef](#)] [[PubMed](#)]

72. Yoo, B.K.; Santhekadur, P.K.; Gredler, R.; Chen, D.; Emdad, L.; Bhutia, S.; Pannell, L.; Fisher, P.B.; Sarkar, D. Increased RNA-induced silencing complex (RISC) activity contributes to hepatocellular carcinoma. *Hepatology* **2011**, *53*, 1538–1548. [[CrossRef](#)] [[PubMed](#)]
73. Perez-Riverol, Y.; Bai, J.; Bandla, C.; García-Seisdedos, D.; Hewapathirana, S.; Kamatchinathan, S.; Kundu, D.J.; Prakash, A.; Frericks-Zipper, A.; Eisenacher, M.; et al. The PRIDE database resources in 2022: A hub for mass spectrometry-based proteomics evidences. *Nucleic Acids Res.* **2021**, *50*, D543–D552. [[CrossRef](#)] [[PubMed](#)]

Disclaimer/Publisher’s Note: The statements, opinions and data contained in all publications are solely those of the individual author(s) and contributor(s) and not of MDPI and/or the editor(s). MDPI and/or the editor(s) disclaim responsibility for any injury to people or property resulting from any ideas, methods, instructions or products referred to in the content.